RADBOUD UNIVERSITY NIJMEGEN

DEPARTMENT: SPECTROSCOPY OF COLD MOLECULES

BACHELOR'S THESIS CHEMISTRY

Optimisation of Molecular Beam Sources
for collision experiments

AUTHOR
S.C. van Lingen

SUPERVISOR
Prof. Dr. S.Y.T. van de Meerakker

SECOND SUPERVISOR
Dr. A. McCollam

July 23, 2018

Preface

When I started the chemistry bachelor program, I did not know which aspect of chemistry I would prefer most. During the courses of my bachelor program, my interest for physical chemistry increased. By mostly following physics courses in the third year of my chemistry bachelor, I decided that I was looking for an internship which combined Chemistry with Physics. Consequently, I found myself at the Department of Spectroscopy of Cold Molecules.

So, at the beginning of February I started my internship on "Optimisation of Molecular Beam Sources". During my internship, I had the luxury of working in the Cold and Controlled Molecules and Ions group at the University of Basel for a couple of weeks. Now at the end of July I am finishing my thesis and I can look back on an enjoyable and educational internship.

I would like to thank my supervisors, T. de Jongh and Prof. Dr. S.Y.T. van de Meerakker, of the Spectroscopy of Cold Molecules group at the Radboud University and my supervisors, Dr. D. Zhang and Prof. Dr. S. Willitsch, at the Cold and Controlled Molecules and Ions group at the University of Basel, for their guidance during this project.

Suzanne van Lingen
July 2018

Contents

Part I

List of Abbreviations

NO	Nitric Oxide
H_2	Hydrogen molecule
p - hydrogen	para-hydrogen
o - hydrogen	ortho-hydrogen
n - hydrogen	75% ortho - 25% para hydrogen mixture
OH	Hydroxide
ICS	Integral Cross Section
DCS	Differential Cross Section
PES	Potential Energy Surface
NPV	Nijmgen Pulsed Valve
ELV	Even Lavie Valve
E_{col}	Collision energy
REMPI	Resonance Enhanced Multi-Photon Ionisation
VMI	Velocity Map Imaging
FWHM	Full Width Half Maximum
PMT	Photo Multiplier Tube
TOF	Time Of Flight
LIF	Laser Induced Fluorescence

Part II
Introduction

With the knowledge of how molecules interact, one can understand chemical reactions in greater detail. Not only in the field of chemistry, but also in physics, molecular interactions are of high interest. For decades, molecular collisions experiments have been key to physicists and chemists in order to obtain a fundamental understanding of molecular interactions.

For performing such molecular collision experiments, molecular beams are used. The first of those were formed just after World War I, when Otto Stern began experimenting with those beams. Since then, molecular beams have improved a lot. To such an extent, that they are nowadays used in many scientific fields. One of which is molecular collision experiments. [1]

The first attempt for molecular collision experiments was performed in the 1960s by Bernstein and partners. [1] However, in the last two decades, collision experiments have improved significantly. Also, the theoretical models are improved, due to the increase of computer power and thereby the improved numerical calculations. These theoretical models can be validated or rejected by the improved molecular collision experiments. [2].

The dynamics of such molecular collision experiments can be described in a classical and a quantum mechanical manner. In classical mechanics a collision between molecules is seen as a collision between pool balls. In this perspective, an incoming pool ball scatters by reflection on a target ball. In quantum mechanics however, the incoming particle is seen as a travelling wave. This wave is scattered by the target, which leads to an interference pattern. [3] For the low energy collisions described in this thesis, the quantum mechanical behaviour dominates. [4] Therefore, we are interested in the quantum mechanical behaviour of the collisions. From this, we can get a better understanding of the interaction between atoms and molecules.

The quality of the data that is obtained by performing a collision experiment depends on the quality of preparation of the collision partners. Therefore, extra attention is paid to the molecular beams.

A molecular beam is produced by a molecular beam source, a so-called valve. The formed beam usually consists of a gas of molecules with approximately equal velocities and few collisions during the flow of the beam. The velocity as well as the properties of the molecules in such a molecular beam can be controlled with beam manipulated methods. Examples of these are the Stark decelerator and Zeeman decelerator [5]. Those manipulation methods in combination with the molecular beams make it possible to control the molecular collisions.

In this thesis, molecular beam sources for two collision experiments are optimised: Crossed molecular beam experiments and trapping experiments. The idea of crossed molecular beam experiments is to collide two molecules by means of molecular beams under a certain angle. Whereas, for trapping experiments, molecules with equal properties are confined in a small area which can be targeted by another molecular beam.

The first part of this thesis focuses on the molecular beams for the crossed molecular beam experiments between NO and H_2 molecules. The H_2 molecule is interesting to study, because it is abundant in nature. Moreover, it is often used as the basis for quantum mechanical descrip-

tions. Collisions between NO and H_2 were already studied at the Department of Spectroscopy of Cold Molecules from Radboud University. In those experiments, collisions were performed at a beam intersection of 45°. Here, collision energies of 14 cm^{-1} were achieved. [3] Recently, the experimental set-up was altered to make a 10° collision angle possible. This makes it possible to go to even lower collision energies ($\sim 2cm^{-1}$) and thereby observe quantum mechanical effects such as scattering resonances (section 2.4). This thesis will specifically focus on the formation of the H_2 and NO molecular beam in order to obtain as low as possible collision energies.

The second part of this thesis is focused on the optimisation of an OH molecular beam for trapping experiments, and was performed at the University of Basel in the Cold and Controlled Molecules and Ions group. In 2013 the group of Parker developed the Nijmegen Pulsed valve (NPV), which was extended with a pin-hole discharge in 2016 to create a radical beam source. [6] [7] In this thesis, a new design for the Nijmegen Pulsed Valve (section 3.2) with pin-hole discharge mechanism (section 3.2.1) was optimised. In these experiments, OH molecular beams are formed because of its essential role in biochemical and atmospheric processes and its extensive usage in molecular collision experiments. The aim of this part of the thesis is to test whether a new design of the NPV equipped with pin-hole discharge with a different shape will lead to improved properties of the valve, such as a higher molecular beam density.

Part III
Theoretical Background

This part of the thesis provides the theoretical background concerning the optimisation of molecular beam sources for a NO, H_2 and OH molecular beam, with the purpose of the beam in mind. First, the molecular properties will be discussed. Subsequently, scattering theories will be examined. Next, a description of the formation of molecular beams is given, which is followed by a section concerning the collision kinematics. This part of the thesis is concluded with the methods used for the detection.

1 Molecular Properties

This section provides a brief quantum mechanical description of the molecules for the molecular beams, that are examined in this thesis. First, properties of the NO molecule are discussed. This is followed by an introduction of the Stark effect. Finally, molecular properties of H_2 and OH are examined.

1.1 The NO radical

The nitric oxide (NO) molecule is called a radical, due to the uncoupled electron in the electronic ground state. This is shown by the electron configuration of the ground state of the NO molecule. In the united atom picture this electron configuration is given by:

$$^{14}N^{16}O\text{: } (1s\sigma)^2(2s\sigma)^2(2p\sigma)^2(2p\pi)^4(3s\sigma)^2(4s\sigma)^2(3p\pi)^1 \tag{1.1}$$

The electron configuration of the ground state yields the electronic orbital ($\vec{L}$) and spin angular momentum ($\vec{S}$). The projections on the nuclear axis of those momenta, $\Lambda = \pm 1$ and $\Sigma = \pm\frac{1}{2}$ respectively, are used to determine the molecular term symbols[1] of the ground state. The corresponding molecular term symbols are the spin-orbit manifolds $X^2\Pi_{\frac{1}{2}}$ and $X^2\Pi_{\frac{3}{2}}$. For NO the $X^2\Pi_{\frac{1}{2}}$ manifold is lower in energy. [3] [10]

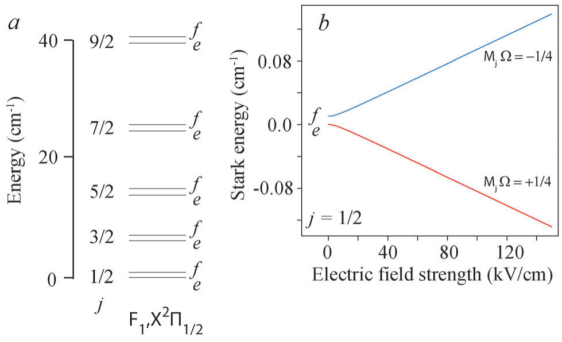

Figure 1: (a) The energy level diagram of the ground state of NO, with the energy splitting of the Λ-doublet of each rotational level. Here the Λ-double splitting is exaggerated for clarity. (b) The Stark shift of the $X^2\Pi_{\frac{1}{2}}(J = 1/2)$ state as a function of the applied electric field strength. (Adapted from reference [8])

The energy level diagram of the ground state manifold, $X^2\Pi_{\frac{1}{2}}$ of NO, is illustrated in figure 1(a). The rotational states (j) consists of Λ-doublet components, denoted with e and f parity. These parities refer to an even or odd wavefunction. The Λ-doubling of the Π-states is a result of the gyroscopic effects on the mixing of the $X^2\Pi$ state with the excited $^2\Sigma$ states. [8] [10] A detailed description of Λ-doubling can be found in reference [10].

[1] Details on the molecular term symbols can be found in reference [9].

1.1.1 Stark Effect of NO

Molecules present in an electric field are subjected to the so-called Stark effect. This is an additional term in the molecular Hamiltonian, given by:

$$H_{Stark} = -\vec{\mu}_{el} \cdot \vec{\varepsilon} \tag{1.2}$$

Here $\vec{\mu}_{el}$ is the electric dipole moment of the molecule and $\vec{\varepsilon}$ is the applied electric field. As a result of the Stark-effect, energy levels shift. This is shown, for the $X^2\Pi_{\frac{1}{2}}(J = 1/2)$ state of NO, in figure 1(b). A state with a positive shift of the Λ-doublet component as a function of the applied electric field is called a low-field-seeking state. Whereas a negative shift is called a high-field-seeking state. High-field-seeking molecules have the tendency to move towards the high electric fields. The e-parity energy level of the $X^2\Pi_{\frac{1}{2}}(J = 1/2)$ state of NO is high-field seeking and will therefore have a tendency to move towards the high electric fields. [5] [8] [10]

More details concerning the Stark-effect can be found in reference [5].

1.2 The H_2-molecule

The hydrogen molecule is the smallest diatom that exists. This makes the hydrogen molecule a basis for many quantum mechanical descriptions of other molecules. In nature H_2 is present in an ortho (75%) - para (25%) mixture (n-hydrogen). The difference in ortho- and para-hydrogen stems from the nuclear spin: [11]

- **Ortho-hydrogen** (o-hydrogen) - The total nuclear spin quantum number **I** = 1.
  Nuclear spin wave-functions: $|\uparrow\uparrow\rangle$, $\frac{1}{\sqrt{2}}|\uparrow\downarrow + \downarrow\uparrow\rangle$, $|\downarrow\downarrow\rangle$.

- **Para-hydrogen** (p-hydrogen) - The total nuclear spin quantum number **I** = 0.
  Nuclear spin wave-functions: $\frac{1}{\sqrt{2}}|\downarrow\uparrow - \uparrow\downarrow\rangle$.

For crossed molecular beam experiments state purity is desired. At room temperature, a thermal equilibrium of 75% *o*-hydrogen and 25% *p*-hydrogen limits the formation of a state pure hydrogen mixture. At a temperature of 20*K* however, a thermal equilibrium of almost 100% *p*-hydrogen is found. [12] Hence, a *p*-hydrogen molecular beam is favoured for these experiments.

Enrichment of *p*-hydrogen is performed by placing *n*-hydrogen in a low pressure chamber containing a para magnetic powder, Nickel(II)Sulfide, at a temperature of 20*K*. This will convert *n*-hydrogen into a 99.9% *p*-hydrogen mixture. [3] The formed *p*-hydrogen cannot be stored in a gas bottle for more than a few days, because it will convert back into an *n*-hydrogen over time. Therefore, *p*-hydrogen is preferred to be formed on the day of the experiment.

1.3 The OH radical

The hydroxide (OH) molecule owes its importance to its role in many biological and atmospheric reactions. Due to the reactivity of the OH molecules, it cannot be stored in a bottle. The reactivity stems from the radical nature of the OH molecule. OH will react with itself or with the walls of the chamber to form a more stable molecule. A way to circumvent this problem, is to form the OH molecules during the beam expansion from water molecules. Methods to obtain OH during the beam expansion include: chemical reactions [13], photodissociation [14],

dielectric barrier discharge [7] and pin-hole discharge [7]. The latter will be used in the experiments described in this thesis and will be further discussed in section 3.2.1.

The OH molecule is a radical, due to its unpaired electron in the ground state, This can be seen from the electron configuration of the OH molecules in the united atom picture:

$$^{16}O^{1}H : (1s\sigma)^2(2s\sigma)^2(2p\sigma)^2(2p\pi)^3 \tag{1.3}$$

From this electron configuration the spin-orbit manifolds $X^2\Pi_{\frac{1}{2}}$ and $X^2\Pi_{\frac{3}{2}}$ for the electronic ground state are derived. For the OH molecule, the spin-orbit manifold $X^2\Pi_{\frac{3}{2}}$ is lower in energy, than the $X^2\Pi_{\frac{1}{2}}$ spin-orbit manifold. The different energy states of these manifolds and the manifold of the first excited state are shown in the energy level diagram, which is provided in appendix A. [15]

2 Scattering Theory

Three different kinds of molecular collisions can be distinguished: elastic scattering, inelastic scattering and reactive scattering. During an elastic collision, the internal energy of the collision partners remains equal, whereas the kinetic energy per collision partner may change while keeping the total kinetic energy equal. In an inelastic scattering process, the internal as well as external energy can change. For both, elastic and inelastic scattering the molecules remain intact, whereas in a reactive collision molecular bonds break and new bonds are formed. [16]

The focus in this thesis is on the inelastic collisions between molecules. This section treats the scattering processes, the angular distributions of collisions and collision probabilities. Finally, the concept of potential energy surfaces and resonances is introduced.

2.1 Classical and Quantum Mechanical Scattering Processes

Scattering processes can be described by means of the angular momentum. In classical mechanics the angular momentum of the colliding particles is given by: $l = |\vec{l}| = |\vec{R} \times \vec{p}| = \mu v_{rel} b$, where μ is the reduced mass and b is the impact parameter as illustrated in figure 2.

The angular momentum in quantum mechanics is quantised and given by: $l = |\vec{l}| = \hbar\sqrt{l(l+1)}$. Here, molecules are considered as travelling waves. The scattering of such waves leads to an interference pattern. The interfering waves are called partial waves. These are defined by a single component of the total angular momentum.

Consequently, if a particle scatters as shown in figure 2, the impact parameter determines the deflection angle, whereas in quantum mechanics the interference is determined by the incident partial waves. Hence, the impact parameter is the classical analogue of a partial wave. [16] [17]

2.2 Differential Cross Section

The differential cross section or DCS, reflects the angular distribution of scattering products.

A schematic view of a particle scattering in a solid angle $d\Omega(\theta,\phi)$ is illustrated in figure 2. The solid angle is defined as: $d\Omega(\theta,\phi) = sin(\theta)d\theta d\phi$, where ϕ is the azimuth angle and θ the polar angle. The differential cross section is described by the number of molecules (dN) that are scattered in a time interval (dt) into the solid angle ($d\Omega$) divided by the total amount of scattered molecules (I). All the solid angles combined lead to the differential cross section, which is given by eq. 2.1. More details can be found in reference [18].

$$\frac{d\sigma}{d\Omega} = \frac{\frac{dN}{d\Omega dt}}{I} = \frac{dN}{d\Omega dt I} \tag{2.1}$$

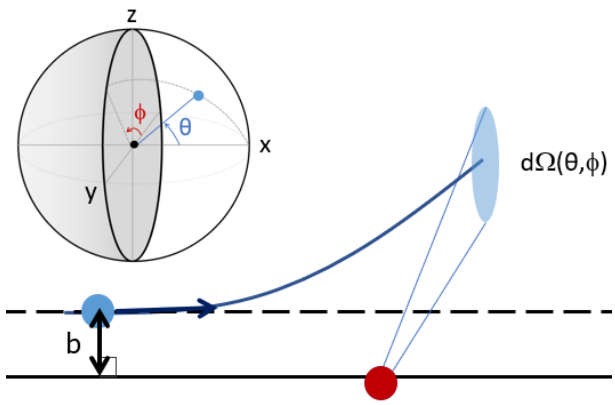

Figure 2: The blue particle scatters on the red particle in the solid angle $d\Omega(\theta,\phi)$. The definition of the impact parameter b, θ and ϕ are shown.

The scattering process has a cylindrical symmetry in ϕ, due to cylindrical symmetry of the experiment. Hence, the DCS is considered as a function of the variable θ. [19]

The definition of the DCS above is defined in the classical picture. In order to form a quantum mechanical description of the DCS, partial waves are used. Let $f(\theta)$ be the partial wave expansion of the interfering states (more details are found in reference [20]), then the DCS is given by: $\frac{d\sigma}{d\Omega} = |f(\theta)|^2$. This implies that the DCS quantum mechanically corresponds to the probability of finding a scattered particle in $d\Omega$. Moreover, the DCS shows the contributing partial waves that make up the interference pattern and thereby contributed to the collision. Consequently, the DCS is a fingerprint for the contributing partial waves. [16]

2.3 Integral Cross Section

The integral cross section (ICS) is an integration over all solid angles of the DCS for a specific collision energy. So, per collision energy the integral cross section is defined as: σ_{tot}, which is given by eq. 2.2. Here $\frac{d\sigma}{d\Omega}$ is the differential cross section. [18] [21]

$$\sigma_{tot} = \oint \frac{d\sigma}{d\Omega} d\Omega = \int_0^{2\pi} d\phi \int_0^{\pi} \frac{d\sigma}{d\Omega} sin(\theta) d\theta \tag{2.2}$$

The integral cross section provides information on the probability of collisions occurring at a certain collision energy. This is dependent on the type of the collision. For an inelastic collision, the kinetic energy of the colliding molecules needs to be high enough to rotationally excite the NO molecules in order to transfer the kinetic energy into rotational energy. When the NO molecules are rotationally excited into a certain state, it is called the opening of that channel.

2.4 Potential Energy Surfaces and Resonances

The aim of molecular collision experiments is to obtain a fundamental understanding of the interaction between atoms and molecules. The interaction between atoms and molecules can be described by means of a potential energy surface (PES). Separation of the rotational motion and the relative radial motion of the molecules lead to the effective interaction potential. Mathematically the effective interaction potential (V_{eff}) can be given by eq. 1.3. Here $V(R)$ is the PES, μ the reduced mass and R the distance between the molecules. The second part of eq. 2.3 leads to the centrifugal barrier, as schematically shown in figure 3. [21] [22]

$$V_{eff}(l, R) = V(R) + \frac{\hbar^2 l(l+1)}{2\mu R^2} \tag{2.3}$$

The bound states of the PES lead to a phenomenon known as resonances. When the collision energy equals the energy of a (quasi-) bound state of the PES a resonance occurs. Thereby, the scattering probability is enhanced, which can be observed with an ICS.

Three kinds of resonances are distinguished:

- **Shape resonances** - These resonances occur when the collision energy is lower than the centrifugal barrier, and tunnelling through the barrier occurs. Furthermore, the initial and bound state are equal. (blue line in figure 3) [16]
- **Feshbach resonances** - These resonances occur, when the bound rotational state corresponds to a higher rotational state than the initial state. This can be seen as a temporary excitation to higher laying rotational state. (red line in figure 3) [16]
- **Shape + Feshbach resonances** - These resonances occur when tunnelling through the centrifugal barrier occurs and the bound state corresponds to a higher rotational state than initial rotational state. (green line in figure 3) [23]

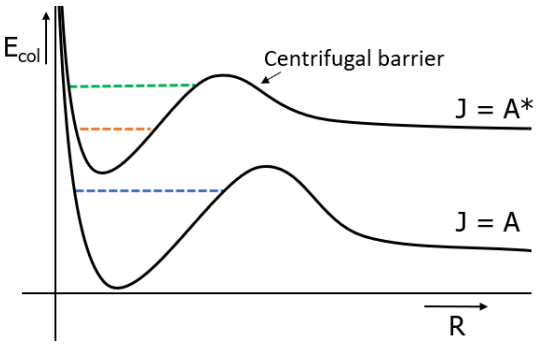

Figure 3: Schematic view of the effective potentials with a centrifugal barrier of the two rotational levels. Here, J=A is higher in energy than J=A. Furthermore, R denotes the distance between the two molecules and E_{col} the collision energy. When the incoming molecules have rotational state J=A the bound states are: blue line - Shape resonance; Red line - Feshbach resonance; Green line - Shape + Feshbach resonance.*

The resonances as described above, strongly depend on full shape of the PES. This fact makes resonances of high interest for collision experiments. [22]

Resonances can be approached from a theoretical point. When solving the Schrödinger equation for V_{eff}, the ICSs can be numerically calculated[2]. Those theoretical predicted ICSs can be compared to the measured data, to check whether the theory is in agreement with the experimental observations. Similarly, the angular distributions can be compared.

For NO-H_2 collisions an ICS measurement of the 1/2e state of NO is performed. Hence, when the collision energy equals the energy of a bound state of the 1/2e potential, it will show a peak in the corresponding ICS. For the measurement of these resonances, a low collision energy is favoured because only a few partial waves contribute to a resonance. These partial waves can be resolved by DCS measurements.

[2]The total wavefunction used for solving the Schrödinger equation is the sum of all contributing partial waves. Detailed quantum mechanical calculations of this concept can be found in reference [20].

3 Molecular Beam Formation

This section elaborates on the formation and manipulation of molecular beams. Specifically, is focused on the molecular beams, for trapping and crossed molecular beam experiments. For trapping experiments, the OH molecular beam is examined. For this purpose, it is important to have a high molecular density and to have state purity of the OH molecular beam. Next, crossed molecular beam experiments with H_2 and NO molecules are examined. For low collision energy crossed molecular beam experiments, state purity of the molecules is desired as well as low velocities and low velocity spreads of the molecular beams.

3.1 Molecular Beam Description

A molecular beam is generally described by a continuous molecular beam. The formation of a molecular beam is illustrated in figure 4. Here, a gas mixture is located in a high pressure chamber. A valve, as indicated in figure 4, makes the connection between the high and low pressure chamber. As a result of the high pressure before the nozzle of the valve (P_0) and the low pressure after the nozzle (P_b, $P_0 \gg P_b$), a molecular beam expansion is formed. [1]

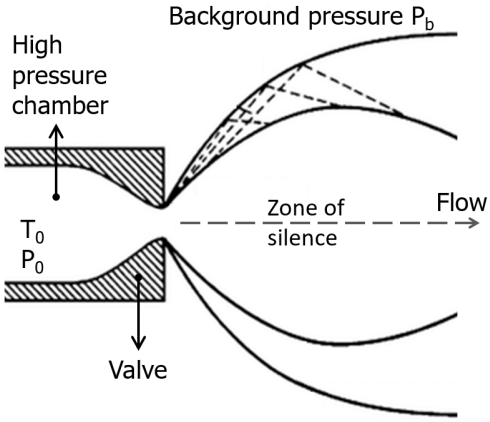

Figure 4: The schematic view of a molecular beam expansion, with P_0 the pressure, T_0 the temperature of the high pressure chamber and P_b the pressure after the nozzle. (Adapted from reference [1].)

When the molecules flow into the low pressure chamber, their kinetic energy is increased. Also, due to the small opening of the valve, lots of collisions occur in the beginning of the expansion of the beam. Therefore, due to conservation of total energy, the internal energy of the molecules is decreased. This leads to nearly all the molecules being in the ground state, which is called adiabatic cooling. [24]

After the molecular beam expansion, no collisions occur around the flow axis. Furthermore, in this part of the beam almost no friction is present. Thereby, this part is called the zone of silence, which is assumed to be an isenotropic region[3]. Hence, the flow of a molecular beam can be described by the use of thermodynamics. The total enthalpy (h_0) is assumed to stay constant along the flow axis in the isenotropic region. Then, by conservation of energy, eq. 3.1 is derived. [1]

$$h_0 = h + \frac{1}{2}mv^2 \iff v^2 = \frac{2}{m}(h_0 - h) \tag{3.1}$$

In this eq. m is the mass, h the enthalpy and v the velocity of the beam along the flow axis. For an ideal gas $dh = C_p dT$, where C_p is the heat capacity. Then, v^2 can be given as an integral, which is dependent on the temperature. Thus v^2 can be defined as eq. 3.2. Here the interval of integration is between the expansion temperature (T_b) and the initial temperature (T_0). [1]

$$v^2 = \frac{2}{m}\int_{T_b}^{T_0} C_p dT \tag{3.2}$$

[3] **Isenotropic region** $\stackrel{d}{=}$ The region in which a gas can flow without changing entropy.

The gas is cooled (due to energy conservation) during the expansion, so $T_0 \gg T_b$. Hence, eq. 3.2 can be approximated by eq. 3.3.

$$v^2 = \frac{2C_p}{m} T_0 \overset{ideal\,gas}{\Longleftrightarrow} v = \sqrt{\frac{2R}{m} \frac{\gamma}{\gamma - 1} T_0} \tag{3.3}$$

Here m is the mass, R the gas constant and λ the isenotropic expansion factor given by: $\gamma = C_p/C_v$ (here C_p and C_v denote the heat capacity at a constant pressure and volume respectively). [1] From eq. 3.3 follows an approximate mean velocity of a molecular beam.

For both trapping experiments and crossed molecular beam experiments, pulsed valves are favoured. This means that a discontinuous molecular beam is used. With a pulsed beam, the whole experiment can be performed on a triggering scheme. Also, these beams are favoured for the usage of manipulation techniques. Moreover, pulsed molecular beams provide well-defined packaged of molecules while the pressure in the chambers remains stable.

3.2 Nijmegen Pulsed Valve

The Nijmegen Pulsed Valve (NPV) consists of a high pressure chamber which contains a controlled leak to a low pressure chamber. This leak is controlled by the opening between the poppet, mounted to an aluminium spring, and the o-ring, which is illustrated in figure 5. By the induced Lorenz force, from a current, the movement of this poppet is controlled. The aluminium spring is bent by this Lorenz force, such that the poppet is lifted up from the o-ring. Hence, an opening is created and the gas can flow through. By this design, the NPV produces short, intense and cold molecular beams. [6]

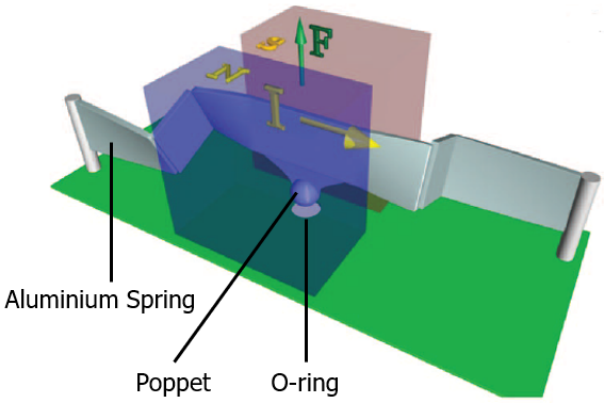

Figure 5: Schematic view of the opening mechanism of the NPV.(Adapted from reference [6])

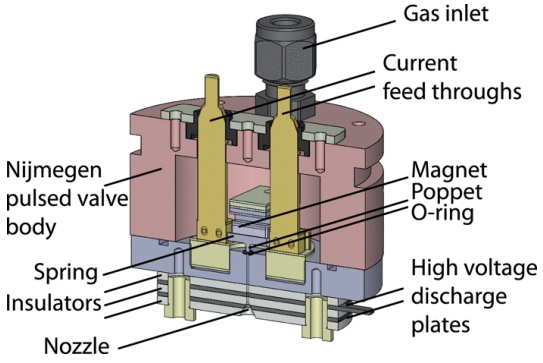

Figure 6: The Nijmegen pulsed valve equipped with a pin-hole discharge. (Adapted from reference [7])

In the experiments described in this thesis, the NO and OH molecular beams are formed with the NPV. For the OH molecular beam, the NPV is equipped with a pin-hole discharge. This is shown in figure 6. The pin-hole discharge will be further emphasised in section 3.2.1. [24]

3.2.1 Pin-hole Discharge

A pin-hole discharge mechanism is used for the production of free radicals during a molecular beam expansion. In figure 7, a schematic view of a pin-hole discharge mechanism is illustrated. Here, the dissociation of H_2O molecules into OH radicals is shown. An electrical current is induced from the metal plate, connected to a negative high electric field, to a ground plate. Thereby, a flow of electrons is created, using the molecules as medium. The electrons collide with the H_2O molecules, which will lead to the dissociation of the H_2O molecules and thereby the formation of the OH radicals.

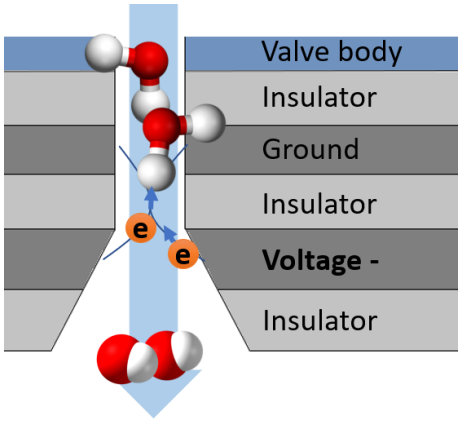

Figure 7: Schematic view of the pin-hole discharge mechanism for the formation of OH radicals. When the current is switched on electrons move from the high voltage plate to the ground plate. The electrons collide with the H_2O molecules, which are flowing downwards, leading to dissociation of the H_2 molecules. Hence, the OH radicals are formed.

Hence, an OH molecular beam can be formed by the dissociation of H_2O by means of the NPV equipped with pin-hole discharge, as illustrated in figure 6. [7]

3.2.2 filament

When using a pin-hole discharge mechanism, a filament can be installed just after the nozzle of the valve. When a current passes through the filament electrons are released and light is visible (figure 8). Because the electrons are close to the discharge mechanism, a filament may help to ignite or stabilise the discharge. [25]

3.3 Even Lavie Valve

The Even Lavie valve (ELV) is used to create the H_2 molecular beam. The ELV is a solenoid valve. This implies that the opening mechanism consists of a plunger inside a coil, that can interact with the magnetic field of the coil. The on and off switching of the magnetic field will lead to the opening and closing of the valve by the movement of the plunger. More information on this valve can be found in reference [26].

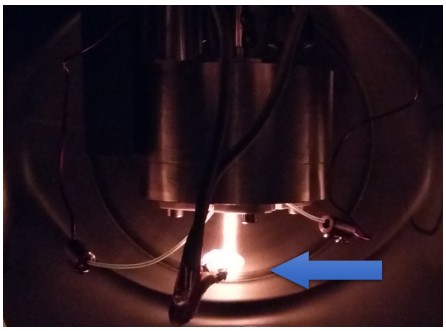

Figure 8: Photograph of the NPV with arrow pointed towards the filament, when the current is on.

Although, the ELV produces molecular beams with favourable properties, it is expensive. A more cost efficient alternative of the ELV is the CRUCS valve.

3.4 Molecular Beam Manipulation

Molecular beam manipulation is important for the crossed molecular beam experiments. In these experiments we want to know what happens during a collision. In order to understand this, the final state of a system is measured and the initial state is controlled. A total control of the incoming molecular beams is thus of high importance for collision experiments. Especially important, is the control of the pre-collision quantum state and velocity.

Moderate quantum state control of a molecular beam can be obtained by a pulsed valve. In the crossed molecular beam set-up the NO molecular beam will be formed with a NPV (section 3.2). This valve makes it possible to adiabatically cool a large percentage of the molecules into the ground state. [24] The H_2 molecular beam is formed with the ELV (section 3.3), because the ELV can be operated at lower temperatures than the NPV. Hence, lower velocity for the H_2 molecular beam can be achieved (eq. 3.3).

In order to obtain low and well-defined energies during a collision experiment, the velocity of the beams as well as the velocity distribution in the molecular beam has to be as low as possible. Options to obtain these velocities include: the use of a seeding gas (section 3.4.1) or deceleration and velocity selection by a Stark decelerator (section 3.4.2).

3.4.1 Binary Gas Mixtures

The mixing of gasses provides a method to moderately control the velocity of a molecular beam. Mixing leads to a different mean mass of the gas. Hence, from eq. 3.3, can be seen that the velocity of the beam will change. When a gas is mixed with a heavier gas, a lower initial mean velocity of the molecular beam is obtained. [1] [27]

This method is also known as the seeding of a gas. This manipulation technique will be used to obtain the desired initial NO molecular beam velocity. For the determination of the average velocity of gas mixtures eq. 3.3 can be used. Here $\overline{C_p}$, the molar average of all the C_p's of the individual gasses, is used instead of C_p and M, the molar average of the masses, is used instead of the single mass m. Also, γ is altered in this way. [1] [27]

Seeding can also be used for the H_2 molecular beam. However, this brings additional complications to the measurements. In section 5 is stated that the detection is performed on the NO molecule. If H_2 is mixed with for instance Neon, H_2 as well as Neon can collide with the NO molecules. Hence, two collision signals are obtained. Therefore, a high detection resolution is needed to differentiate between those signals. This makes seeding of the H_2 beam not a favourable method, if low collision energies can be reached by other means.

3.4.2 Stark Decelerator

A molecular beam can be controlled by the Stark decelerator, as shown in figure 9. The Stark decelerator is used for deceleration, velocity selection, transversal and longitudinal velocity focusing and state selection of the molecular beams. It makes use of high voltage fields to decelerate and focus molecules with an electric dipole moment. This deceleration process is especially effective when the molecule has a large dipole moment. [5]

The Stark decelerator consists of electrode pairs with alternating high voltage and ground, as shown in figure 10. When a molecule enters the potential field, the kinetic energy of the molecule decreases. However, the potential field is sinusoidal. Therefore at a certain point the molecule gains kinetic energy. Before the molecule reaches that point, the field is switched off and the field of the next stage is switched on. Again the molecule loses kinetic energy. This process is repeated for multiple stages until the desired velocity is obtained. [5]

Although this deceleration technique is not effective for molecules with a small dipole moment, the Stark decelerator is used because of its other properties: 1. minimisation of transverse and longitudinal velocity spread and velocity selection and 2. the state selection of molecules.

Figure 9: Picture of the Stark decelerator. (Adapted from reference [24])

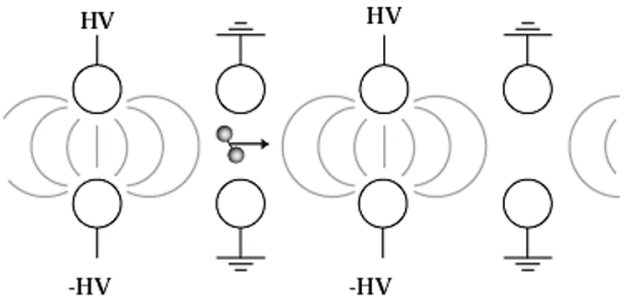

Figure 10: Schematic view of a molecule passing through the electrode pairs of the Stark decelerator. (Adapted from reference [5])

1) The Stark decelerator will be used to select a velocity of the NO molecular beam for the collision. Velocity selection as well as the transverse and longitudinal focusing of the molecular beam is dependent the timing of the Stark decelerator with respect to the incoming NO molecular beam. In order to obtain the desired properties of the NO molecular beam the s = 3 and $\phi_0 = 0$ modes of the Stark are used. Details of this concept can be found in reference [5].

2) The Stark decelerator is used to select the $X^2\Pi_{\frac{1}{2}}(J = 1/2, f)$ state of the NO radical (section 1.1). Before the NO molecules enter the Stark decelerator, the molecules are mainly in the electronic rotational ground state but in both parities. Due to the electric fields, the difference in the energies of the e and f-parity states is increased. The Stark decelerator only allows the low-field seeking states to pass. Hence, the exiting molecules are only low-field seeking. [5]

4 Kinematics of Collision Experiments

By describing the kinematics of the experiment, the collision energy as well as the collision energy resolution can be calculated from the properties of the molecular beams. First the elastic collision experiments are considered. Subsequently, inelastic collisions are discussed.

4.1 Determination of the Collision Energy

For the description of the collision experiments it is common to use two different kinds of reference systems:

- **The Centre of Mass frame (CM-frame):** The CM-frame has the centre of mass as the origin of the system and only considers the relative motion of the particles.
- **The Laboratory frame (Lab-frame):** The Lab-frame is considered as the frame in which the experiment is performed and is therefore is stationary.

It is convenient to describe the kinematics in the CM-frame for collision experiments. Whereas, the Lab-frame is related to the actual experiment. Therefore, a clear relation between those frames is needed.

Let A and B be particles with mass m_A and m_B and velocity $\vec{v}_A$ and $\vec{v}_B$. Denote the total mass M = $m_A + m_B$, then the velocity of the centre of mass ($\vec{v}_{CM}$) is given by: $\vec{v}_{CM} = \frac{m_A \vec{v}_A}{M} + \frac{m_B \vec{v}_B}{M}$. The velocities of particle A and B in the Lab-frame can be given in terms of the $\vec{v}_{CM}$ and the velocities of A and B in the CM-frame, $\vec{u}_A$ and $\vec{u}_B$ respectively (eq. 4.1).

$$\vec{v}_A = \vec{v}_{CM} + \vec{u}_A \text{ and } \vec{v}_B = \vec{v}_{CM} + \vec{u}_B \tag{4.1}$$

Define the relative velocity as $\vec{v}_{rel} = \vec{v}_A - \vec{v}_B = \vec{u}_A - \vec{u}_B$. Then $\vec{u}_A$ and $\vec{u}_B$ can be expressed in terms of the relative velocity and the masses m_A, m_B and M. Note that the total momentum $\overrightarrow{P_{tot}} = m_A\overrightarrow{u_A} + m_B\overrightarrow{u_B}$ equals zero in the CM-frame. Then, $\vec{u}_A$ and $\vec{u}_B$ are given by eq. 4.2.

$$\vec{u}_A = \frac{m_B \vec{v}_{rel}}{M} \text{ and } \vec{u}_B = \frac{m_A \vec{v}_{rel}}{M} \tag{4.2}$$

For collisions experiments, the collision energy is of high importance. The collision energy is equal to the initial kinetic energy of the system in the CM-frame. When particle A collides with particle B the collision energy (E_{col}) is given by eq. 4.3

$$E_{col} = \frac{1}{2}\mu \vec{v}_{rel}^2 = \frac{1}{2}\mu[v_A^2 + v_B^2 - 2v_A v_B cos\alpha] \tag{4.3}$$

Where $\mu = \frac{m_A m_B}{m_A + m_B}$ is the reduced mass of the system and α the collision angle. From eq. 4.3 follows that the collision energy decreases, with decreasing relative velocity. Hence, the lowest collision energy is obtained for minimal relative velocity. [3] [18] [19]

4.2 Energy Resolutions

The collision energy resolution is of high importance in order to differentiate between resonances. Before performing a collision experiment, the resolution of the collision energy can be approximated.

Variations in v_A, v_B and α will lead to variations in the collision energy. The spread in the collision energy can be given by the differential of eq. 4.3, yielding eq. 4.4.

$$dE = \mu\{(v_A - v_B cos\alpha)dv_A + (v_B - v_A cos\alpha)dv_B + v_A v_B sin\alpha d\alpha\} \tag{4.4}$$

The standard deviation (σ) of v_A, v_B and α is used to determine the spread in collision energies. Assumed is that all variation are Gaussian distributions. The full width half maximum of quantity i is denoted by $\Delta_i = 2\sqrt{2ln(2)}\sigma(i)$. Then, by error propagation, the collision energy spread (Δ_E) is given by eq. 4.5. [28]

$$\Delta_E = \{\mu[(v_A - v_B cos\alpha)^2\Delta_{v_A}^2 + (v_B - v_A cos\alpha)^2\Delta_{v_B}^2 + (v_A v_B sin\alpha)^2\Delta_\alpha^2]\}^{\frac{1}{2}} \tag{4.5}$$

From eq. 4.3 follows that if $\alpha = 0°$ or $\alpha = 180°$ the term $2v_A v_B cos\alpha$ is maximal. Therefore, the collision energy with respect to the angle is minimal. From eq. 4.5 follows that for $\alpha < 90°$, the minimal collision energy spread can be obtained. Consequently, the minimal collision energy and collision energy spread are obtained for $\alpha = 0°$. For the experimental set-up described in this thesis, a collision angle of zero degrees is difficult to achieve. Hence, the experiments are performed with a beam intersection of 10°.

Furthermore, it is concluded, from eq. 4.3 and eq. 4.5, that a low value for $|v_A - v_B|$ leads to a low value for E_{col} and Δ_E. Also, a low velocity spread of v_A and v_B will lead to a lower spread in Δ_E.

To make the concept of energy resolution more clear, the collision energy resolution of a NO-H_2 experiment is calculated with eq. 4.5. Here, v_{H_2}, α and all Δ_i are kept constant and v_{NO} is varied. Let $v_{H_2} = 800m/s$, $\alpha = 10°$ and $v_{NO} \in [500 : 900]$ m/s. Then the theoretical energy resolution as shown in blue in figure 11 will be obtained. Also, in this figure the velocities of the NO beam as a function of collision energy are shown in red. The same conclusions, as discussed above, can be derived from figure 4.5.

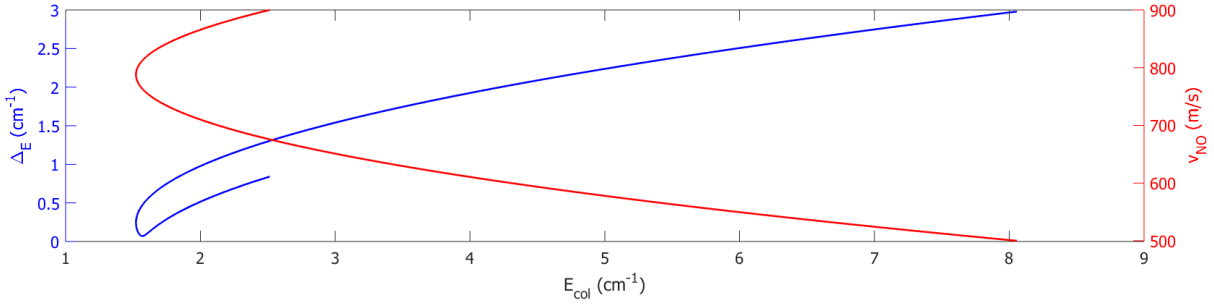

Figure 11: Blue: The Energy resolution as a function of the collision energy. Red: the velocity of the NO molecular beam as a function of the collision energy. Here $v_{H_2} = 800m/s$, $\alpha = 10°$ and $v_{NO} \in [500, 900]m/s$.

4.3 Newton Diagram

So far the kinematics before the collision are treated. This section will discuss the situation after the collision. For this a so-called Newton diagram is used.

A Newton diagram of the scattering process shows the conservation of energy. Such a diagram contains pre- and post-collision velocity vectors. An example of a Newton diagram for an elastic scattering process in illustrated in figure 12. Here a collision between particle A and particle B is illustrated. For the particle i, the mass is denoted m_i, the initial LAB-velocity is $\vec{v}_i$ and $\vec{u}_i$ is the velocity in the CM-frame. The collision angle is denoted with α and the origins of the frames are denoted O_{LAB} and O_{CM}. The *prime* indicates the post-collision velocity vectors.

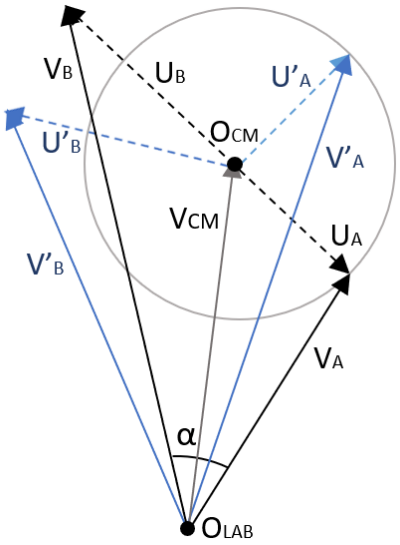

Figure 12: The Newton diagram for a two-dimensional elastic scattering process between a particle A and B.

In figure 12, a Newton sphere for particle A is constructed. The construction consists of a circle with the centre of mass as centre and a radius of length u_A. During elastic collisions the momentum is conserved so $u_A = u'_A$. The collisions examined in this thesis are inelastic. In an inelastic collision part of the kinetic energy is transferred to internal energy or vice versa. Hence, the momentum before the collision differs from the momentum after the collision. Therefore the radius of the Newton sphere will be altered. This radius can be calculated by using the internal energy uptake or release of the system, which is shown in eq. 4.6. [1] [19]

$$u'_A = u_A \sqrt{1 - \frac{\Delta E}{E_{col}}} \tag{4.6}$$

Here $\Delta E = E'_{int} - E_{int}$ represents the energy uptake or energy release, where E_{int} is the total internal energy of the system before the collision and E'_{int} is the total internal energy of the system after the collision. Experimentally, a Newton sphere is measured in order to determine the differential cross section (section 2.2).

5 Detection Methods

For the optimisation of molecular beam sources, different detection methods are used depending on the beam in question.

The OH molecular beam is detected by means of a microphone and laser induced fluorescence. In the crossed molecular beam experiments, the NO molecules are detected after the collision. The NO molecules can state selectively be ionised by the use of a REMPI scheme. The detection of the ionised NO molecules is performed with the technique Velocity Map Imaging, developed by Eppink and Parker (1997). [29]

The different detection methods described above are discussed in this section.

5.1 Microphone

A microphone provides a simple method to measure a beam profile at a desired location. The differences in the pressure at the position of the microphone lead to different resistances in the microphone. These resistances can be translated to the intensities of the molecular beam passing the microphone. Hence, a molecular beam profile is obtained.

5.2 Laser Induced Fluorescence

Laser Induced Fluorescence (LIF) makes it possible to sensitively detect a specific state of a molecule. A laser is used to excite electrons from a specific electronic state to an energy level from which fluorescence occurs. Subsequently, this fluorescence is detected.

For the detection of the OH molecular beam, LIF is especially useful. A LIF excitation scheme for the OH molecules is illustrated in figure 13. A Nd:YAG pumped dye laser, with 282 nm, excites the electrons from the $X^2\Pi_{\frac{3}{2}}(v=0)$ state to the $A^2\Sigma^+(v=1)$ state. Due to the short lifetime of the $A^2\Sigma^+(v=1)$ state, the electrons decay to the $X^2\Pi(v=1)$ state causing fluorescence. The induced fluorescence has a wavelength of 313 nm. Hence this fluorescence functions as a measure for the amount of OH molecules in a specific electronic state. This can be used to estimate the percentage of OH molecules in the ground state but also for the measurement of a beam profile. [15] [19]

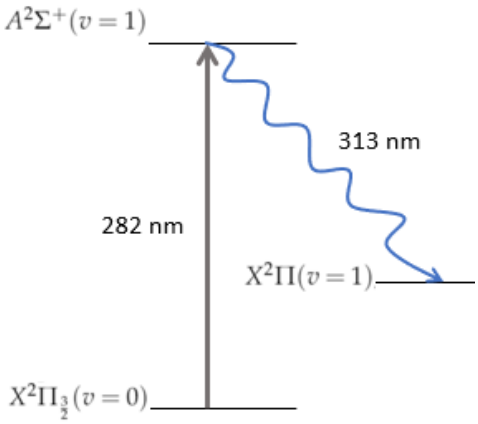

Figure 13: The induced fluorescence (313 nm) caused by the excitation from the $X^2\Pi_{\frac{3}{2}}(v=0)$ to the $A^2\Sigma^+(v=1)$ state.

In figure 13, off-diagonal LIF is performed. The reason for this is the Franck-Condon overlap of the energy levels in question. Due to the small Franck-Condon overlap, decay from the $A^2\Sigma^+(v=1)$ state leads to a different wavelength than the wavelength of the excitation laser. The advantage of the off-diagonal LIF is thus the minimised interference of the excitation laser during the detection.

5.3 REMPI Scheme

Resonance Enhanced Multi-Photon Ionisation (REMPI), is a technique that state specifically ionises molecules.

For the ionisation of the NO molecules a (1+1′) REMPI scheme is used. This is schematically shown is figure 14. In the (1+1′) REMPI scheme two photons, with different wavelengths, are used to state selectively ionise the NO molecules. For this purpose, two different dye lasers are used, which are both pumped by the same Nd:YAG laser. The molecules are first state selectively excited by the first dye laser, with a wavelength depending on the transition from the specific rotational state of the $X^2\Pi$ manifold to the $A^2\Sigma^+$ manifold. The second dye laser has a wavelength of $327.7nm$, and is used to ionise NO from the $A^2\Sigma^+$ manifold. [8] [30]

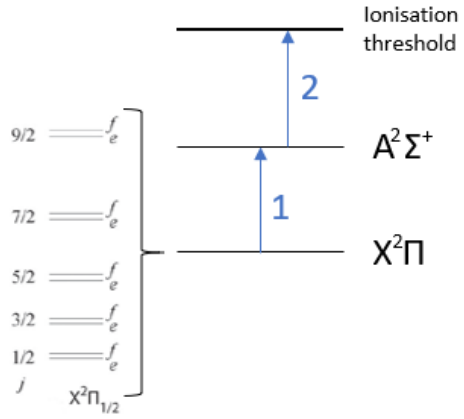

Figure 14: The (1 + 1′) REMPI scheme used for the detection of NO. Here laser 1 excites the NO of the rotational excited $X^2\Pi$ state to a $A_2\Sigma^+$ rotational state and laser 2 ionises the excited NO.

Note that the wavelength of the second laser is tuned just above the ionisation threshold. This prevents ion recoil, which can occur when the NO molecules have more energy than is needed for ionisation. This excess energy can be transferred into kinetic energy, which leads to different final velocities of NO during the measurement. Hence ion recoil makes the measurement less accurate. [8]

Specifically, the (1+1′) REMPI scheme will be used to ionise NO from the 1/2f, 1/2e or the 3/2e state (figure 14). NO molecules exiting the Stark decelerator are mostly in the $X^2\Pi(J = 1/2), f$ state. When the NO molecules collide with H_2 molecules the electrons may go into other energy states. By performing (1+1′) REMPI on 1/2e and 3/2e states of the collision signal, the background signal of the 1/2f molecules is reduced. For the measurement of the initial NO beam (1+1′) REMPI on the 1/2f state is performed.

5.4 Velocity Map Imaging

Velocity Map Imaging (VMI) provides a unique method to visualise the post-collision velocity vectors as a function of the scattering angle.

Schematically, the VMI set-up is illustrated in figure 15. The lasers are aligned such that the overlap section of the lasers is located in the detection region. Also, the molecular beams are aligned such that the collisions take place in the cross section of the lasers and thereby the detection region. Here, the NO molecules are excited and ionised by means of the (1+1') REMPI scheme (section 5.3). The charged molecules are repelled by an electrostatic field created by a repeller plate. The repulsion forces the molecules in the direction of the detection screen. An electrostatic lens is created by the three extractor plates, with a 20 mm diameter hole. The voltages of these plates are set to meet the VMI conditions (see reference [29]). Hence, the molecules are focused such that molecules, with different positions but equal velocities with respect to the repeller plate, will have the same position on the detection screen. Before the molecules are detected, they go through a grounded time-of-flight tube of 550 mm length, to shield the molecules from any electric or magnetic fields. With this set-up molecules with equal post-collision velocity vectors, will give a signal on the same location on the detection screen. Thus, VMI provides the detection of the Newton sphere for a collision process. [8] [29]

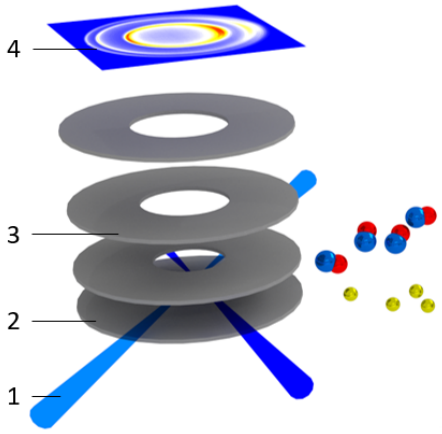

Figure 15: Schematic view of the VMI set-up used in the collision experiments consisting of: 1. Laser, 2. repeller plate (U_{rep}), 3. extractor plates (U_{E_i}) and 4. the detection screen.

The detection screen consists of three parts: *1.* MCP screen *2.* phosphor screen *3.* CCD camera. First, the molecules will hit a microchannel plate (MCP). This MCP sends out electrons on the other side of the screen, but at the same position. Those electrons will hit a phosphor screen. The phosphor screen generates light by means of luminescence, which is subsequently detected by a CCD camera. The position of the light is detected by the CCD camera and thereby represents the impact position of the NO molecules, which is largely governed by the underlying DCS. [8] [29]

Part IV
Experimental Techniques

The experimental part of this thesis consists of two parts. First, the experimental techniques concerning the optimisation of the H_2 and NO molecular beams for crossed molecular beam experiments are discussed. Secondly, the experimental techniques for the optimisation of the NPV, with newly designed pin-hole discharge are examined.

6 Optimisation of the H_2 and NO Molecular Beam

The experimental set-up used for the crossed molecular beam experiments, for NO-H_2 collisions, is illustrated in figure 16. The NO molecular beam is formed with a NPV at a frequency of 10 Hz and a backing pressure of 1 bar (section 3.2). The NO beam enters a low pressure chamber, with a pressure kept below $2.2 \cdot 10^{-6}$ mbar by a Pfeifer turbo pump. Subsequently, the NO beam goes through a skimmer[4] of 3mm diameter. Next, the molecules enter the Stark decelerator (section 3.4.2) of 317 electrode pairs with a 36kV difference between the opposing electrons. The desired velocity of the NO molecules is selected and longitudinal and transverse focusing takes place. Directly after exiting the Stark decelerator the NO molecules enter a hexapole[5] for additional transversal focusing. This hexapole is added to make the 10° beam intersection angle possible. Then, the NO molecules arrive at the collision area. The H_2 molecular beam is formed with the ELV in a separate source chamber, after which the molecules go through a 2mm skimmer and enter the collision area. The lasers are aligned such that the collisions occur in the overlap region of the dye lasers. Therefore, the NO molecules are excited and ionised by the usage of a REMPI scheme. Finally, the NO molecules are detected with VMI (section 5.4).

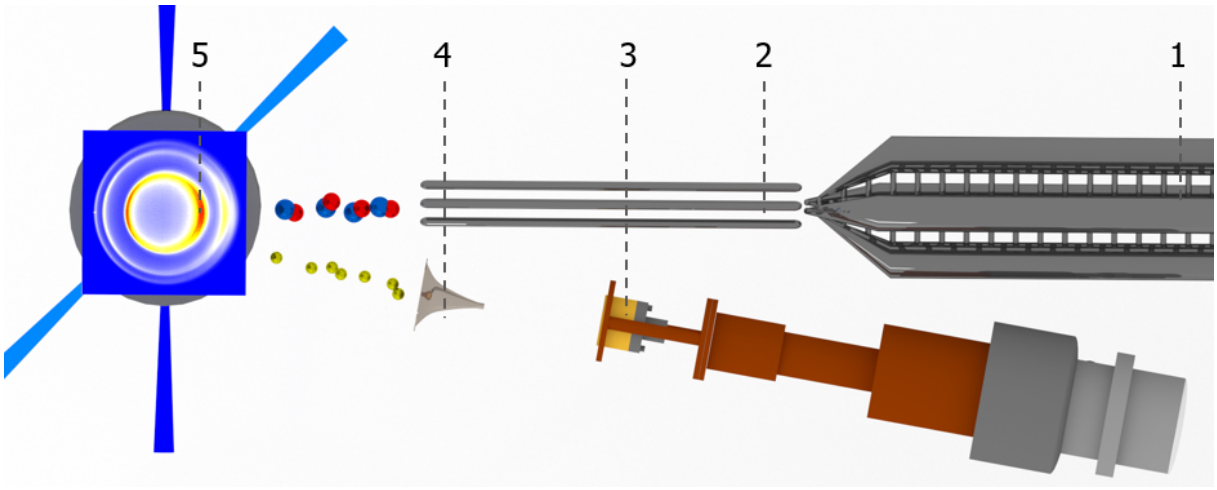

Figure 16: The schematic overview of the collision region of the experimental setup, for collision experiments at a beam intersection 10°, containing: 1. Stark decelerator, 2. the hexapole, 3. the ELV for the H_2 molecular beam, 4. Skimmer, 5. the VMI set-up as shown in figure 15.

[4] A skimmer is an object which is conically shaped and placed on the flow axis of the molecular beam. This will lead to the centre part of the beam being extracted of the molecular beam.

[5] A more detailed description of a hexapole can be found in reference [5].

For the optimisation of the H_2 and the NO molecular beam the triggering scheme as shown in figure 17 is used. First, a trigger is sent to open the NPV. Then, when the molecules enter the Stark decelerator, the high fields of the Stark are triggered. When the molecules exit the Stark decelerator, the hexapole is triggered. The ELV is triggered before the laser and the detection camera.

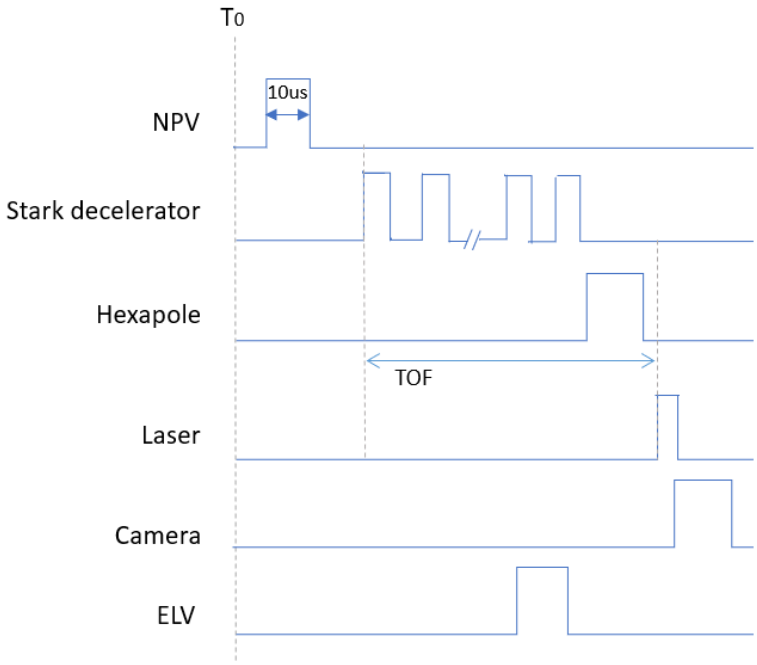

Figure 17: The triggering scheme which is used for the crossed molecular beam experiments. Also, shown is the timing used for the Time Of Flight scan (TOF) for the NO molecular beam.

In figure 17, the timing for a so-called time of flight measurement (TOF) for the NO molecular beam, is shown. For a TOF measurement, a scan is made for the different timings of the triggering of the laser with respect to the first stage of the Stark decelerator. By this measurement beam profiles of the molecular beam are obtained.

With the experimental set-up discussed above, the NO and H_2 molecular beams are optimised. First the possibilities with the H_2 molecular beam are studied and optimised. From the properties of the H_2 molecular beam, the desired conditions and gas mixtures for the NO molecular beam are derived using eq. 3.3, 4.3 and 4.5 and tested. From all the above information, the optimal beams for performing collision experiments with NO and H_2 are determined. With those molecular beams, collision experiments are performed and an ICS and angular distribution are measured.

6.1 Simulations

A crossed molecular beam experiment can also be simulated by means of a Monte Carlo simulation (see reference [31]). To test whether the theory is in agreement with the measured data, a simulated angular distribution is formed by using the theory as an input for the Monte Carlo simulation. By doing this, experimental effects are also included in the theory. Subsequently, the simulation provides the theoretical angular distribution, which can be compared to the measurements.

7 Optimisation of the new NPV with Pin-hole Discharge

A new design for the NPV with pin-hole discharge was tested. In figure 18 the original pin-hole discharge configuration and the newly designed configurations are illustrated. In the new design, the straight channel is removed and a replaced by a full cone shape. Configuration 1 has a high voltage applied to the first plate (counted from the valve body along with the flow direction), and the discharge is directed towards the valve body. For configuration 2 the high voltage applied to the plate second plate, and the discharge is directed towards the ground plate.

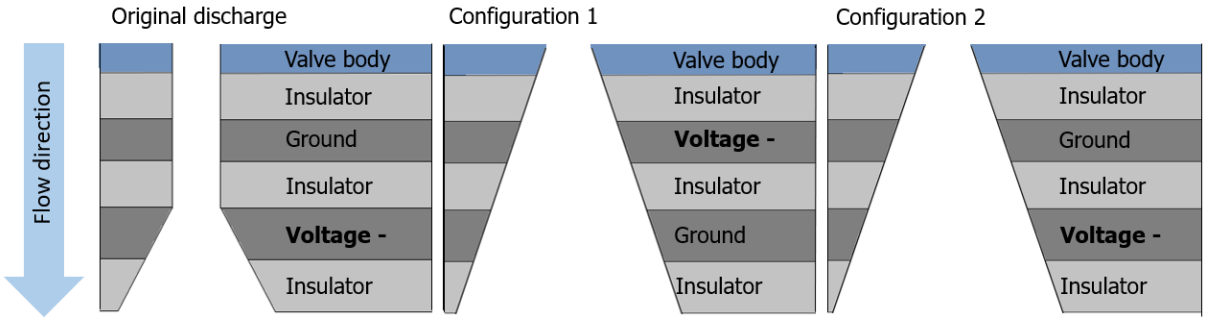

Figure 18: Left, a schematic view of the normally used configuration of the pin-hole is illustrated. Right, the new pin-hole discharge configurations 1 and 2, which differ in the location of the high voltage (negative voltage) and ground.

The angle of the opening of the new NPV with pin-hole discharge is 50°, which was found to be the optimal angle by Even (2014). [32] The thickness of each of the plates is 1 mm, which makes the diameter of the first metal plate 3 mm and the diameter of the second metal plate 8 mm.

The discharge mechanisms are tested in a vacuum chamber, of which the set-up is shown in figure 19. The valve is placed vertically (z-direction) inside the test chamber, which is vacuum pumped by a molecular turbo pump to approximately $7 \cdot 10^{-7}$ bar. In the xy-plane (25.25cm from the nozzle) an excitation dye laser passes through to a Brewster window, which functions as polarisation selector for the laser, when entering or exiting the vacuum chamber. This is followed by light baffle after which it excites the molecular beam. Then the laser goes through another light baffle followed by another Brewster window after which the laser power can be measured. The laser excites the molecules from the $X^2\Pi_{3/2}(v = 0)$ ground state to the first excited $A^2\Sigma^+(v = 1)$ state. Also, in the xy-plane a Photo Multiplier Tube (PMT) is placed perpendicular to the laser beam axis. The PMT functions a detector for the emitted photons of a weakly emitting source. The PMT is equipped with a lens and two filters (an interference filter with a bandwidth around 20 nm and an UG11 interference filter) which are used to filter out the stray light from the excitation laser.

Figure 19: The test chamber containing: 1.NPV with pin-hole discharge, 2.PMT, 3.laser path consisting of Brewster windows and light baffles and 4.microphone.

The NPV was operated at a frequency of 20 Hz and the OH molecular beam was formed by dissociating the H_2O molecules, which were seeded in Argon. In the experiment, LIF signals were measured (see section 5.2). For the measurements of the beam profiles, the LIF signal was integrated for varying trigger delays of the laser pulse (figure 20). Also, a microphone was placed in the test chamber with a distance of 50.89 cm from the nozzle, in order to determine the velocity of the OH molecular beam.

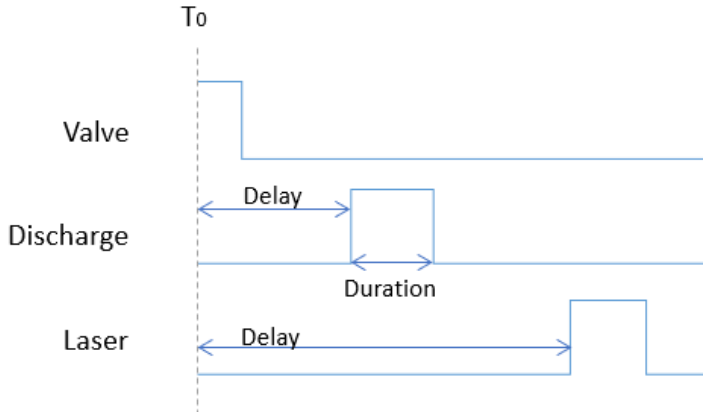

Figure 20: The triggering scheme which is used for the test chamber.

For the optimisation of the new valve the triggering scheme in figure 20 was used. First, a trigger is sent to open the valve. Then, the discharge is triggered after which OH radicals are created. Finally, when the molecules arrive at the detection region, the excitation laser is triggered.

Before the optimisation of the new NPV with pin-hole discharge, the LIF signal was measured in order to approximate the lifetime of the $A^2\Sigma^+(v=1)$ state of OH. Then, the beam profile was measured using the microphone to determine the velocity of the beam. The procedure for the optimisation of configuration 1 and 2 entails optimising the following parameters: discharge delay, discharge duration, backing pressure and discharge voltage. Finally, a tungsten filament (operated at an optimised current of 0.7 A) was installed just after the nozzle of the NPV. After which the effect of the filament on the discharge voltage was measured. With the optimal conditions and the filament, a rotational resolved electronic spectrum was measured in order to determine the percentage of molecules in the electronic rotational ground state.

Part V
Results and Discussion

8 Optimisation of the H_2 and NO Molecular Beam

Performing crossed molecular beam experiments requires the optimisation of the molecular beams in question. Therefore, the NO and H_2 molecular beams are optimised for low collision energy experiments. The NO molecular beam is used in previously performed crossed molecular beam experiments, for instance reference [33]. Hence, information on the possibilities with this molecular beam is available. Also, because the velocity selection of the Stark decelerator is very precise, the velocity of the NO molecular beam can be accurately set. Consequently, the possibilities with the H_2 molecular beam are first examined. Subsequently, the NO molecular beam is optimised to suit the desired properties. Finally, collision experiments are performed and an ICS and an angular distribution are measured.

8.1 The H_2 Molecular Beam

A low collision energy requires molecular beams with a minimal velocity. According to eq. 3.3, $v \propto \sqrt{T}$. Hence, vapour pressure data was used to determine the lowest temperature at which the gas would not freeze. In figure 21 the vapour pressure data of H_2 is shown. The H_2 beam is formed with the ELV, which is operated at a pressure of 2 bar. Consequently, the minimum temperature to be reached is 23K. For measurements at an operating temperature of the ELV (T_{ELV}) of 23K the pressure is lowered to 1.2 bar for additional prevention of freezing.

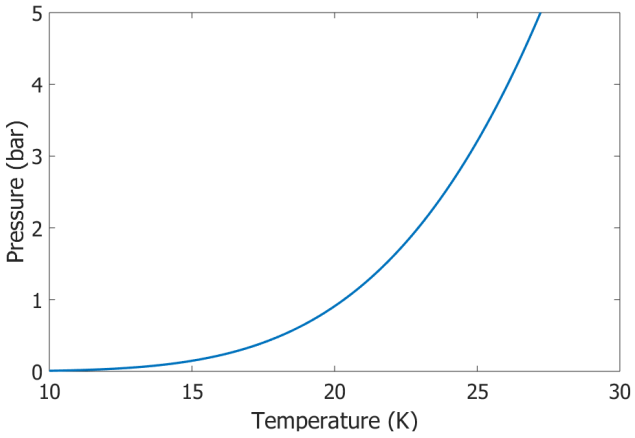

Figure 21: The vapour pressure against the temperature for H_2. The data was adapted from reference [34].

The ELV was cooled down to $T_{ELV} = 23K$ and TOF profiles for $T_{ELV} \geq 23K$ were measured. These profiles were measured by means of collisions, because no direct measurement option was present. The H_2 molecules collided with NO (v_{NO}=670 m/s, NO selected by the Stark decelerator from a *5%NO-95%Ar* gas mixture), at different timings with respect to the trigger of the ELV. In figure 22 these TOF profiles for the optimised conditions[6] per temperature are shown. A behaviour of decreasing relative intensity with decreasing velocity is observed. The lowest relative intensity is thus found at a temperature of 23K, but the relative intensity is still sufficient for collision experiments.

In order to measure resonances at the lowest collision energies, a temperature of 23K is needed. However, for measuring an energy region such as for an ICS, other collision energies are also needed. Hence, a less critical temperature for the ELV is favoured, because this provides a

[6]The optimisation consists of optimising the backing pressure and the opening time op the ELV.

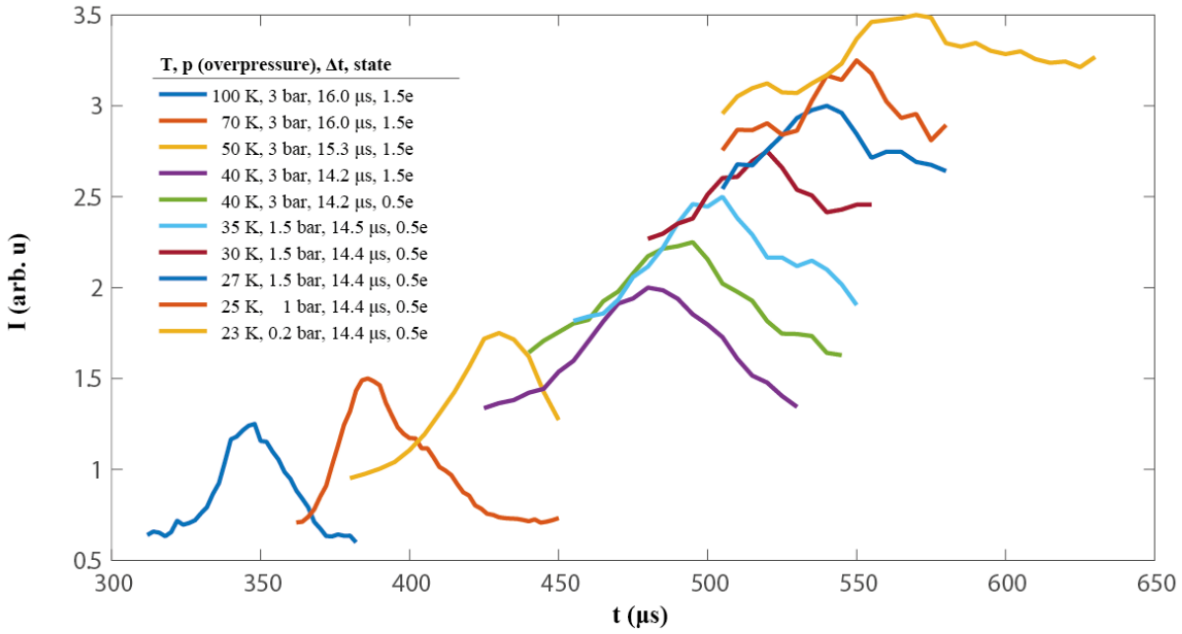

Figure 22: The TOF profiles of H_2 for the different settings for the Even Lavie valve, with differing temperatures, backing pressure and opening times. The time represents the time from the trigger of the ELV to the detection point. The TOF profiles are shifted upwards for a clearer view. All TOF profiles are measured by collisions with v_{NO}=670 m/s, which is selected from a 5%NO-95%Ar gas mixture by the Stark decelerator.

molecular beam with a higher relative intensity. Therefore, the measurements at higher collision energies will be performed at 28*K*.

8.1.1 Energy Calibration for the Velocity

It was stated that no direct measurement option is present to measure the H_2 molecular beam. Hence, the opening of the 3/2e channel is measured, in order to determine the velocity of the H_2 molecular beam. For the operating temperature of 23*K* and 28*K* the real velocity of the H_2 molecular beam is determined by collisions with a *5%NO-95%Ar* gas mixture. In principle, an $E_{col} \in [4,8]cm^{-1}$ can be reached (eq. 3.3 and 4.3). With this data the opening of the 3/2e channel[7] can be measured.

In figure 23 measurement of the opening of the 3/2e channel for $T_{ELV} = 28K$ is shown. Also the theoretically predicted ICS of the 3/2e channel is shown in blue. [35] The obtained collision data forms a s-curve around $E_{col} \cong 5cm^{-1}$. This is observed due to the velocity spread in the

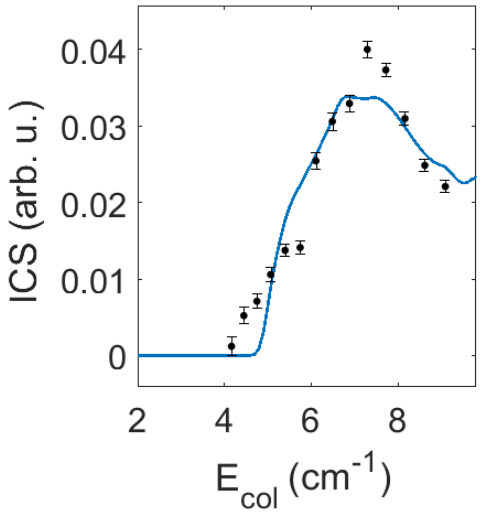

Figure 23: The measurement of the opening of the 3/2e channel of the NO molecule for $T_{ELV} = 28K$. The measured collision energies correspond to the NO velocities of 530 m/s to 660 m/s. The blue curve is the theoretically predicted ICS from reference [35].

[7] A collision energy of $\sim 5cm^{-1}$ is needed for the opening of the 3/2e channel.

molecular beams and thereby a spread in collision energies (section 4.2). The middle of this s-curve, corresponds to the overlap of the mean velocities of the beams and thereby to the opening of the 3/2e channel of NO. Using the measured collision energies and the corresponding velocities of the NO beam ($v_{NO} \in [530,660]$), the velocity of H_2 could be calculated using eq. 4.3. Also, the measured collision energies are fit to the ICS signal to the expected opening of the channel in order to approximate the velocity of H_2. Therefore, the velocity of the H_2 molecular beam at$T_{ELV} = 28K$ was concluded to be 850 m/s. The same approach was used for $T_{ELV} = 23K$. At this temperature a velocity of $v_{H_2} = 800$ m/s was found.

Next to the mean velocity of the H_2 molecular beam, the velocity spread along the flow axis is determined. A reliable method to approximate the order of this velocity spread is to determine the spread in the collision energy, which is found by the above described s-curve ($\sim 0.3cm^{-1}$). From the collision energy an approximation of the velocity spread is made by using eq. 4.5. The found velocity spread of the H_2 molecular beam has an order of magnitude of 10 m/s.

For a more detailed determination of the velocity and velocity spread of the H_2 beam, the lasers have to be altered to perform REMPI on the H_2 molecule. The precise velocity and velocity spread will be measured in the near future.

8.2 The NO Molecular Beam

For the measurement of the lowest and the higher collision energies of H_2 with NO, a wide range of NO velocities is needed. Therefore, the use of different NO gas mixtures is essential. Furthermore, during each set of measurements, the velocity of the H_2 molecular beam needs to be determined. Hence, for each NO gas mixture, another gas mixture is required to calibrate on the 3/2e channel. For the 1/2e and 3/2e ICS measurements an $E_{col} \in [1.5,10]cm^{-1}$ is preferred, in order to compare the measured data to the theoretical ICSs. [35]

Gas mixture				Mean velocity (via eq. 3.3) [m/s]	Mean velocity [m/s]	FWHM [m/s]	Velocity range [m/s]
%NO	%Ne	%Ar	%Kr				
5	95			847	840	120	[780,900]
5	65	30		747	760	120	[680,820]
5	35	60		675	680	120	[580,620]
					600	60	[620,760]
5		95		613	660	120	[550,600]
					560	100	[600,700]
5		47.5	47.5	530	-	-	[430,630]

Table 1: Overview of the measured molecular beams with their calculated mean velocity from eq. 3.3 with $T = 350K$, measured mean velocity, FWHM and the velocity range of the gas mixture. For the latter gas mixture the lowest velocities were not determined.

In order to obtain $E_{col} \in [1.5,10]cm^{-1}$, several gas mixtures that contain 5%NO are tested (5%NO was found to be optimal in reference [3]). First, Eq. 3.3 was used to estimate the

mean velocities of possible molecular gas mixtures[8]. The most suited gas mixtures are shown in table 1, with their calculated mean velocity, measured mean velocity and corresponding full width half maximum (FWHM) and the velocity range. For several gas mixture two measured mean velocities are shown. This emerged from an observed two peak structure in the neutral molecular beam[9].

The first aim is to find a gas mixture in which a velocity of 800 m/s, and thereby a minimal collision energy, is achieved. For this purpose TOF profiles of the neutral molecular beam and the selected velocities of the first three gas mixtures of table 1 were measured. For the *5%NO-35%Ne-60%Ar* and *5%NO-95%Ne* gas mixtures a velocity of 800 m/s was obtained. For both mixtures however, the contrast between the intensity of the selected velocity and adjacent velocities is very low. Therefore, these gas mixtures are inadequate for a minimal collision energy measurement. For the *5%NO-65%Ne-30%Ar* gas mixture however, a clear TOF profile around 800 m/s is found, which makes this molecular beam suitable for collision experiments with H_2 molecules. An overview of the TOF profiles of the selected velocities and neutral beam as a function of the delay at the detection region of this gas mixture is illustrated in figure 24.

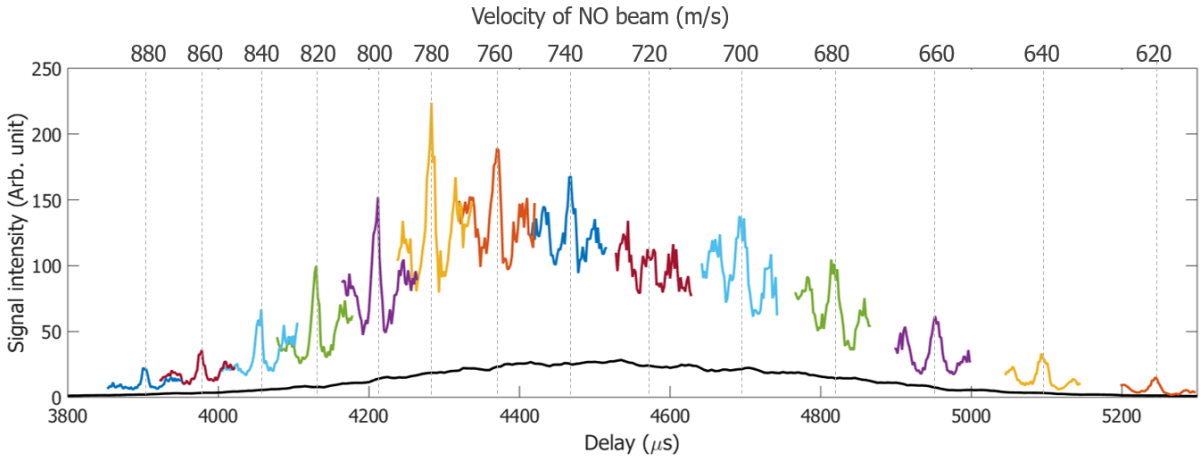

Figure 24: Overview of the TOF profiles of the selected velocities by the Stark decelerator of the 5%NO-65%Ne-30%Ar gas mixture. Black: The intensity of the molecular beam without velocity selection as a function of detection time. Coloured: The TOF profiles of the individual selected velocities by the Stark decelerator (and hexapole), from which the velocities are shown on the upper x-axis. (30 avg.).

The TOF profile for $v_{NO} = 800$ m/s is shown in figure 24 and shows great contrast between the intensity of the selected velocity and adjacent velocities of the molecular beam. Hence, this gas mixture makes it possible to measure at the lowest collision energies. Also, a small width of the velocity selected TOF profiles compared to the non-selected beam profile is observed. Due to the velocity selection of the NO molecular beam by the Stark decelerator the velocity spread is small, which is favourable for the collision energy resolution.

As a conclusion, the *5%NO-65%Ne-30%Ar* gas mixture with $T_{ELV} = 23K$, will be used for the collision experiments around $E_{col} \in [1.5, 2.4] cm^{-1}$ (eq. 3.3). For the opening of the 3/2e channel, and thereby the determination of v_{H_2}, a gas mixture of *5%NO-47.5%Ar-47.5%Kr* will be used. Because, $v_{NO} \in [430, 630]$ colliding with $v_{H_2} \cong 800$ m/s will in principle lead to $E_{col} \in [3.5, 11.7]$,

[8]For the estimation of the possible molecular gas mixtures, a velocity spread of 100 m/s for the initial NO molecular beam was kept in mind.

[9]Neutral beam $\stackrel{d}{=}$initial produced molecular beam without the Stark decelerator

which covers the range for the measurement of the opening of the 3/2e state of NO.

With the above settings we are able to measure the lowest desired collision energies. However, with these settings not the whole collision energy range for the 1/2e and 3/2e ICS can be measured. Hence, other settings are needed to fill this gap. For the above settings the H_2 valve is operated at $T_{ELV} = 23K$. When the valve is operated at $T_{ELV} = 28K$, different collision energies can be reached and different NO gas mixtures may be needed. Because small differences in signal intensity may occur, due to slight changes in the environment between measurements. It is needed to create some overlap of the collision energies per measurement day or by the use of a different gas mixture. Also, for each different temperature a gas mixture for the 3/2e measurement is needed. In order to achieve these requirements, the gas mixtures indicated in table 2 are concluded to cover the collision energy range, $[1.5, 10]cm^{-1}$.

Gas Mixture				Collision Energy Range $[cm^{-1}]$	T_{ELV}
%NO	%Ne	%Ar	%Kr		
5	65	30		1.5 – 2.4	23K
5		47.5	47.5	3.5 – 11.5	23K
5	65	30		1.7 – 3.6	28K
5		95		3.2 – 8.2	28K

Table 2: Overview of the gas mixtures, that are used to cover the collision energy range from 1.5-11.5cm^{-1}, with overlap of collision energies between the mixtures taken into account. An operating temperature of 25*K leads to* $v_{H_2} = 800$ *m/s and* 28*K leads to* $v_{H_2} = 850$ *m/s.*

Table 2 provides the molecular beams needed to measure in the desired collision energy range. Hence, the collision energies are sufficiently low, to measure the lowest resonances. Therefore, the seeding method described in section 3.4.1 is not used for the H_2 molecular beam, because it would lead to an unnecessary more complicated analysis. Subsequently, with the settings of table 2, the first ICS and DCS were measured. This is shown in the following sections.

8.3 ICS Measurement

The ICS shows the chance of colliding as a function of collision energy (section 2.3). In order to determine an ICS, three different measurements are performed:

- **Overlap signal** - In this measurement the number of NO molecules, after the collision, are measured in the desired state (1/2e or 3/2e state of NO).
- **Non-overlap signal** - This is a measure for the background signal. The Stark decelerator is used as state selector for the NO molecule. However, some imperfections may occur. This means that a fraction of the molecules exiting the Stark decelerator, are not in the $X^2\Pi_{\frac{1}{2}}(J = 1/2, f)$ state (section 3.4.2). Therefore, some molecules are in the desired state while exiting the Stark decelerator. In order to correct for this phenomenon, this background fraction is measured. This measurement is performed with the same conditions as for the Overlap signal, but without colliding.
- **Beam density** - This is a measure for the amount of NO molecules that are present in the selected velocity of the NO molecular beam. The importance of this correction can be seen

in figure 24. Here, the 620 m/s selected velocity peak, shows a much lower intensity than the 780 m/s velocity peak. So, for 620 m/s less molecules are present prior to colliding. Hence, a correction for this observation is needed.

From those three measurements the total scattering signal (ICS_i) can be determined by performing the following calculation for each measurement point, i:

$$ICS_i = \big((Overlap\ signal)_i - (Non\text{-}overlap\ signal)_i\big) \,/\, (Beam\ density)_i \tag{8.1}$$

The overlap signal, non-overlap signal, and beam density measurements were performed for the 1/2e channel. These were measured with a *5%NO-95%Ar* gas mixture, $T_{ELV} = 28K$ and a *n*-hydrogen gas mixture. A pulse duration of $\Delta t = 14.7\mu s$, trigger start point of $t_{ELV} = 2475\mu s$ was used for the ELV at an operating pressure of 2 bar. Furthermore, the ion optics were defocussed.

From these measurements the ICS was determined. The results of this are plotted together with a theoretical prediction of the ICS (multiplied with a normalisation factor of $9.3527e-5$ and convoluted with an energy spread of $0.5cm^{-1}$) in figure 25. [35] Also, a so-called Density-to-Flux correction was performed on the measured ICS. This correction takes into account the interaction time between the two molecular beams, further information on this correction can be found in reference [36].

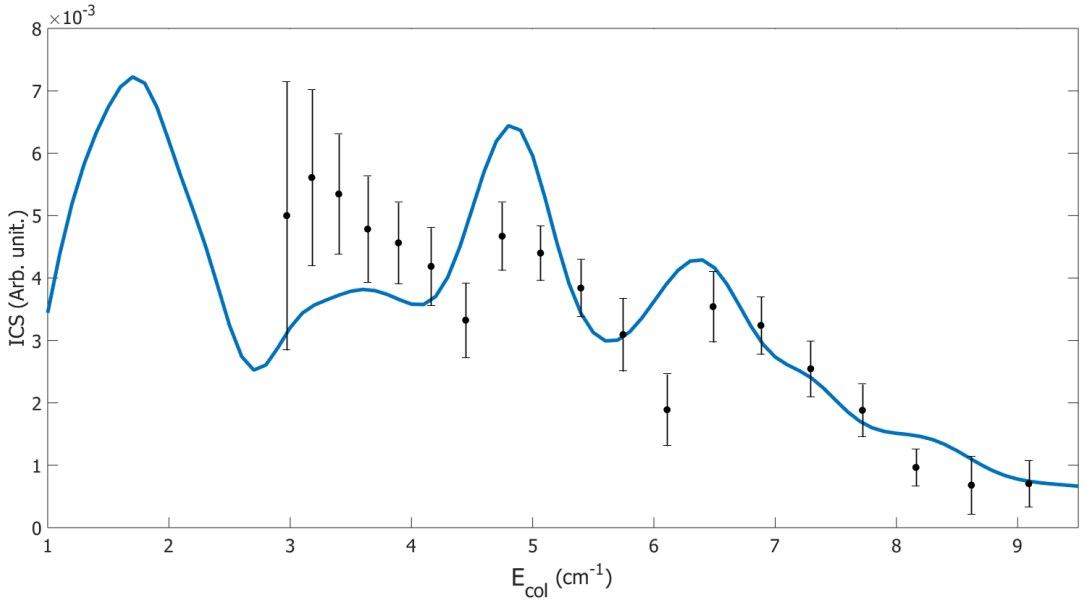

Figure 25: The measured ICS of the opening of the 1/2e channel. This spectrum is measured for collisions between NO in the 5%NO-95%Ar gas mixture with n-hydrogen. The blue curve shows the theory for this system with a normalisation factor of $9.3527e-5$. *Furthermore, the theory is convoluted with a Gaussian, with FWHM=*$0.5cm^{-1}$. *This theory was determined in reference [35]. (1 avg, #step=501)*

Figure 25, shows that $E_{col} \in [3,9]cm^{-1}$ was achieved. This is in correspondence with the approximate collision energy range from table 2. The theory is in agreement with the data for the higher collision energies, E_{col}>$5.5cm^{-1}$. For the lower collision energies, the theory shows small deviations from the measured data. The data shown in figure 25, is one of the first ICS measurements for these collisions. Hence, experimental improvements are possible. Also, better suited theories need to be developed.

8.4 DCS Measurement

For the measurement of the angular distribution of scattering products VMI was used. A DCS is measured at one collision energy. This means that only one velocity of NO is used to collide with the H_2 molecules.

An angular distribution of the scattering between NO ($v_{NO} = 660$ m/s) and n-hydrogen ($v_{H_2} = 850$ m/s) was measured, with ELV settings $T_{ELV} = 28K$, $\Delta t = 14.7\mu s$, $t_{ELV} = 2480\mu s$ at an operating pressure of 2 bar. The result of this measurement is shown in figure 26. Here, the forward direction[10] of NO is directed towards the right. The collision energy of this angular distribution is approximately $4.2cm^{-1}$. This angular distribution, shows a clear decreased signal intensity at a scattering angle of 90°. The fact that we are able the observe such structures in the angular distribution, while the number of averages is quite low and two kinds of collisions occur (o- and p-hydrogen), forms a promising prospect for DCS measurements with p-hydrogen.

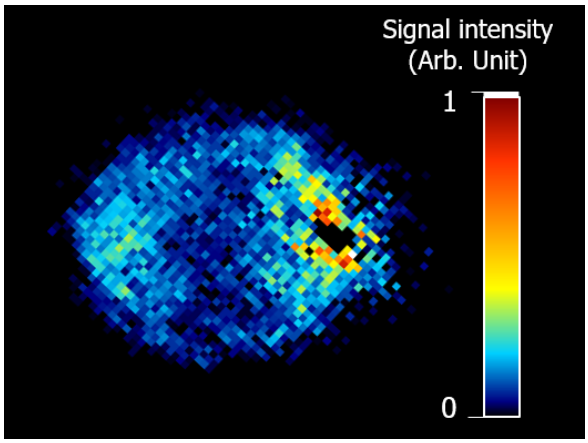

Figure 26: The measured DCS for collisions between NO and n-hydrogen. Here v_{NO} =660m/s, which is selected from a 5%NO-65%Ne-30%Ar gas mixture. Here, the forward direction of NO is directed towards the right. The graph was averaged over 25.000 laser shots

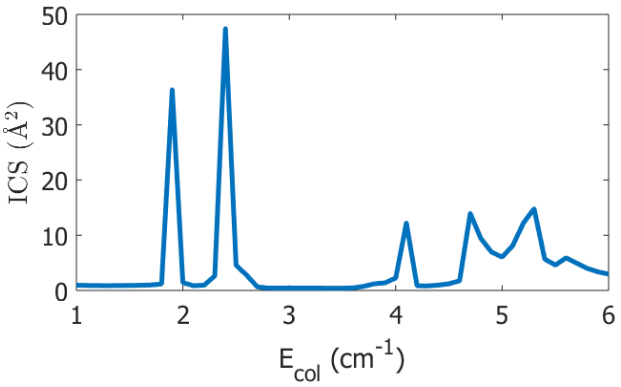

Figure 27: The theoretically predicted ICS of the 1/2e channel of NO colliding with p-hydrogen. This ICS is calculated with the potential from reference [35].

8.5 Simulations from Theory

For different collision energies, angular distributions of NO colliding with p-hydrogen were simulated by means of the Monte Carlo simulation (section 6.1). The predicted theory was used as an input for the simulations. [35] The simulated angular distributions are shown in figure 28. Here the velocity of p-hydrogen is kept constant, whereas the velocity of NO is altered to obtain the collision energy. Furthermore, the forward direction of NO is directed towards the right. The corresponding theoretical prediction of the ICS for the 1/2e state is illustrated in figure 27.

In figure 28 is observed that the radius of the angular distribution of the scattering products increases with increasing collision energy. This phenomenon can be understood with the use of a Newton diagram (section 4.3). The radius represents the final velocity of NO in the CM-frame (eq. 4.6). Because, only the velocity of the NO molecular beam is altered, a change in collision

[10]Forward direction $\stackrel{d}{=}$ direction of the initial velocity vector in the CM-frame.

energy can be translated to a change in the final velocity of NO molecular beam. Consequently, the change in collision energy can be translated to a change in the radius.

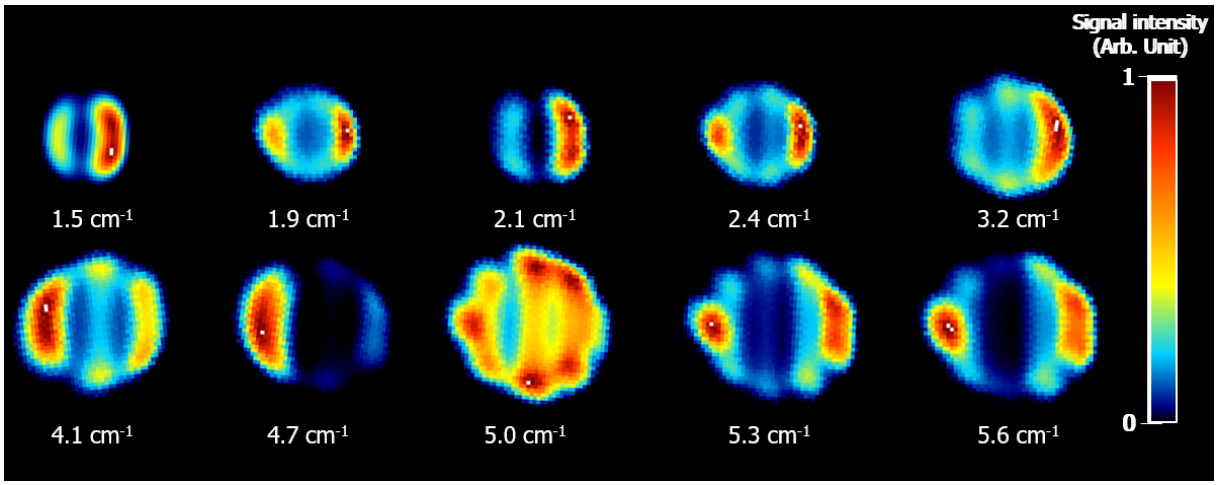

Figure 28: Simulated angular distributions of scattering products for different collision energies. Here the forward direction of the NO molecules is directed towards the right. The signal intensities belonging to the different colours are given by the colour bar, here white corresponds to a high signal, blue to a low signal and in between the signal intensity is linearly interpolated. The velocity of p-hydrogen is kept constant: $v_{H_2} = 800$ m/s, whereas the velocity of NO is altered from 560 m/s to 800 m/s. For the input of the simulated DCSs, the theory from reference [35] was used.

More important are the patterns, which are visible in the angular distributions. These patterns are characteristic to the wavelike nature of the collision. This can already be observed by the clear shift in the patterns in the angular distribution on the resonances (peaks in figure 27). Also, can be seen that for lower collision energies the patterns are simpler and therefore it seems that less partial waves are contributing to the DCSs at lower collision energies.

In order to validate the used theory for *p*-hydrogen, the ICS and angular distributions of scattering products will be measured in the near future.

9 Optimisation of the new NPV with Pin-hole Discharge

A new design for the pin-hole discharge mechanism is optimised for trapping experiments. First, a LIF signal is measured and the molecular beam velocity is determined. Subsequently, configuration 1 will be optimised (figure 18). Optimisation of the pin-hole discharge consists of optimising the following parameters: discharge delay, discharge duration, backing pressure, discharge voltage and the effect of a filament. The same parameters are optimised for configuration 2. Finally, for both configurations a rotationally resolved spectrum is measured, and is compared to the original pin-hole discharge design.

9.1 Configuration 1

First, the LIF signal of the OH molecular beam was measured. The measured LIF signal is shown in figure 29. An exponential fit of the measured signal is shown in red. From this fit a the lifetime of the $A^2\Sigma^+$(v=1) state is approximated to be 780 $\pm$ 1.6e-2 ns, which is in accordance with previous measured lifetimes of this state of OH (reference [7], [37]).

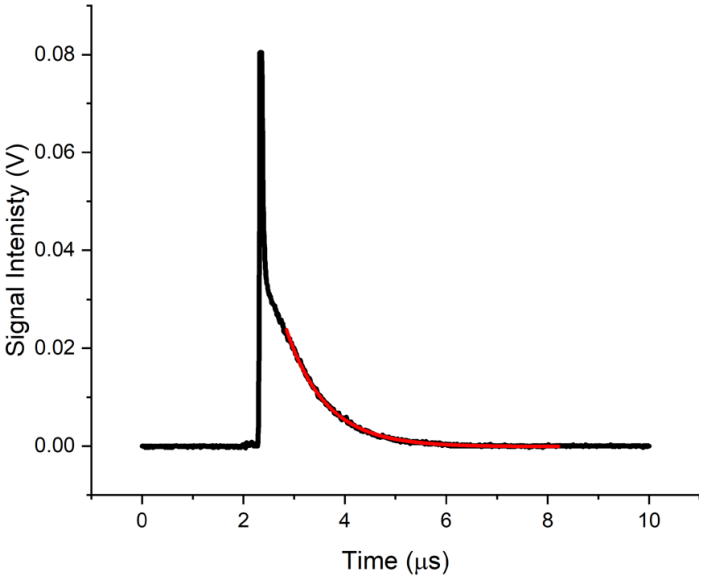

Figure 29: The measured LIF signal of the molecular beam. The red line shows the exponential fit. The approximated lifetime of OH is 780 $\pm$ 1.6e-2 ns. The signal was measured with a discharge delay of 50 µs, discharge duration of 20 µs, 920 V, backing pressure of 1 bar and 0.9 mJ laser power (384 avg.)

Subsequently, a profile of the molecular beam was measured by the microphone. The results of these measurements are illustrated in figure 30. The highest intensity of the beam profile is found at 689 μs. This combined with the distance of 0.5089m from the nozzle gave a mean beam velocity of 739 m/s with a FWHM of 114 m/s.

The first variables that were optimised are the discharge delay and discharge duration. The beam profiles of the OH molecular beam with varying discharge duration were measured for a discharge delay of 40 μs, 45 μs and 50 μs. These profiles are shown in figure 32. For the LIF-based beam profiles a higher beam density corresponds to a more negative signal intensity. Hence, from figure 32 becomes clear that for a discharge delay of 45 μs the lowest signal intensity is obtained. Furthermore, from these graphs it is clearly visible that a lower discharge duration corresponds to a smaller peak width. Additionally, when comparing the minima of the discharge delays a clear shift is observed. For a higher discharge delay, the minimum is found at later at the laser overlap region. This observation originates from the formation of the OH molecules. For a discharge delay of 50μs the OH molecules are created later compared to molecules created at a discharge delay of 40μs. Because the molecules have approximately equal velocities, the last created OH molecules arrive last in the laser overlap region. During this optimisation procedure the molecular beam with the highest beam density, highest stability and lowest velocity-spread is desired. Hence, from the above follows that a discharge delay of 45 μs and a discharge duration of 20μs is best suited for trapping experiments.

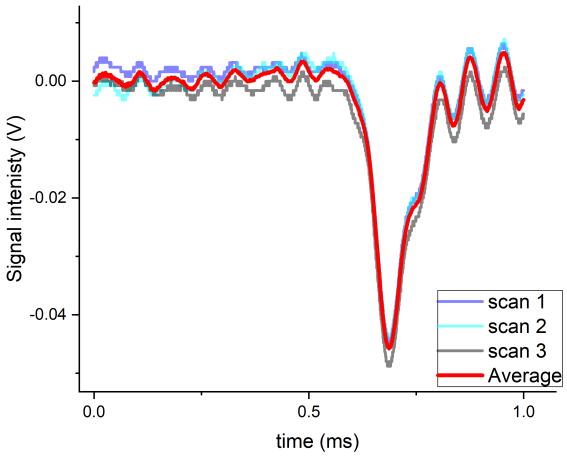

Figure 30: The beam profiles without the discharge taking place. 3 measurements of 128 avg. were performed, from which also the average is illustrated in red. The backing pressure was 0.5 bar.

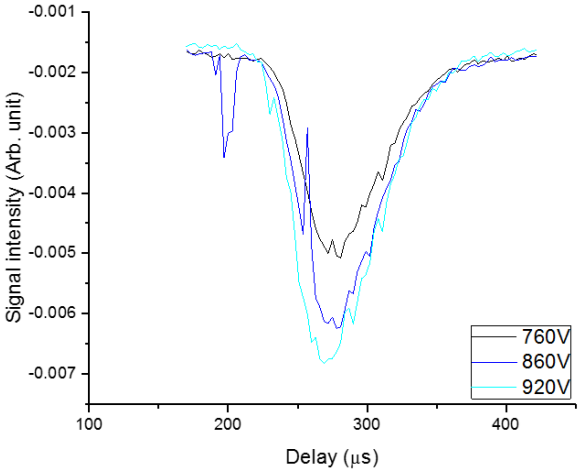

Figure 31: The voltage dependence of configuration 1. Measured at a discharge delay of 45 µs, a discharge duration of 20 µs, 0.5 backing pressure and 0.9 mJ laser power (64 avg.)

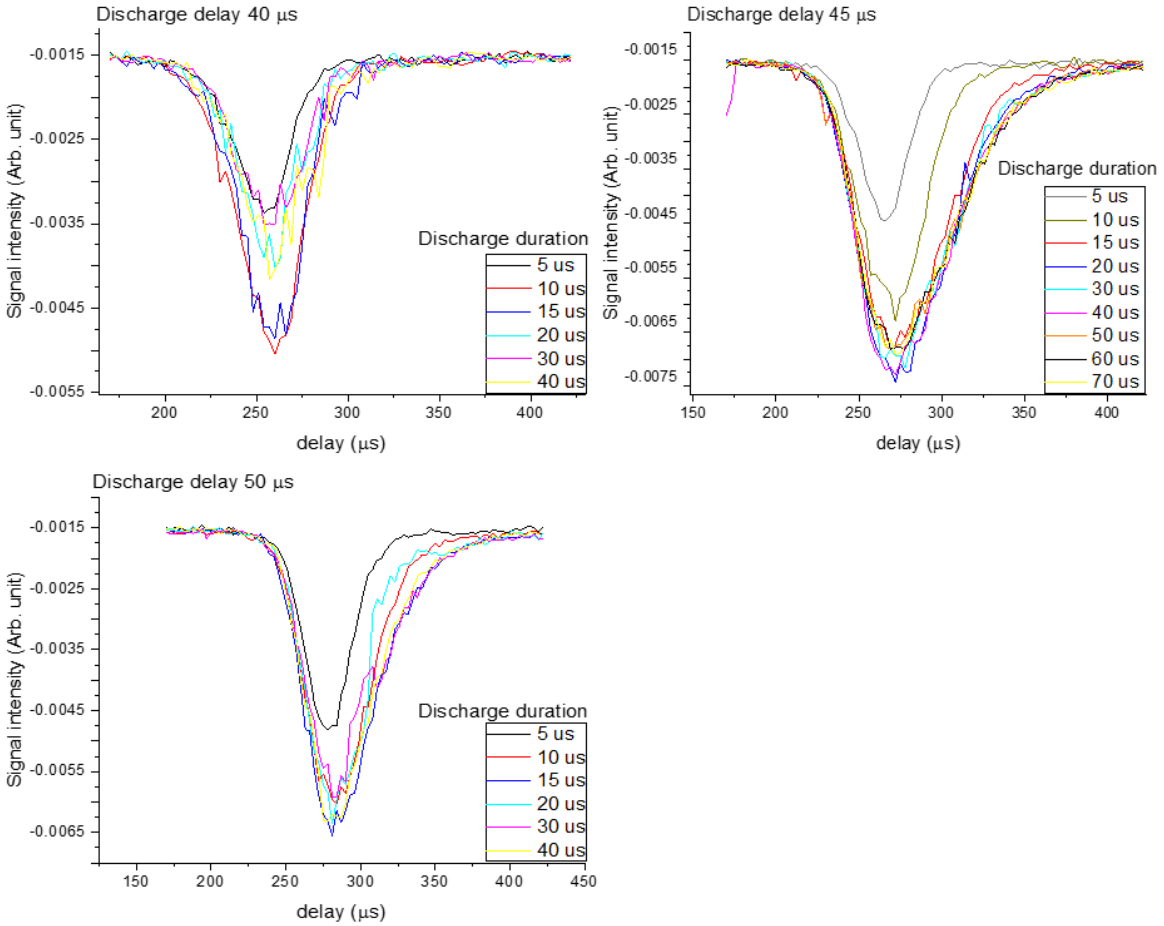

Figure 32: Overview of the discharge delay with varying discharge duration for configuration 1. The signals were measured with a backing pressure of 3.5 bar, 920 V and a laser power of 0.9 mJ (64 avg.).

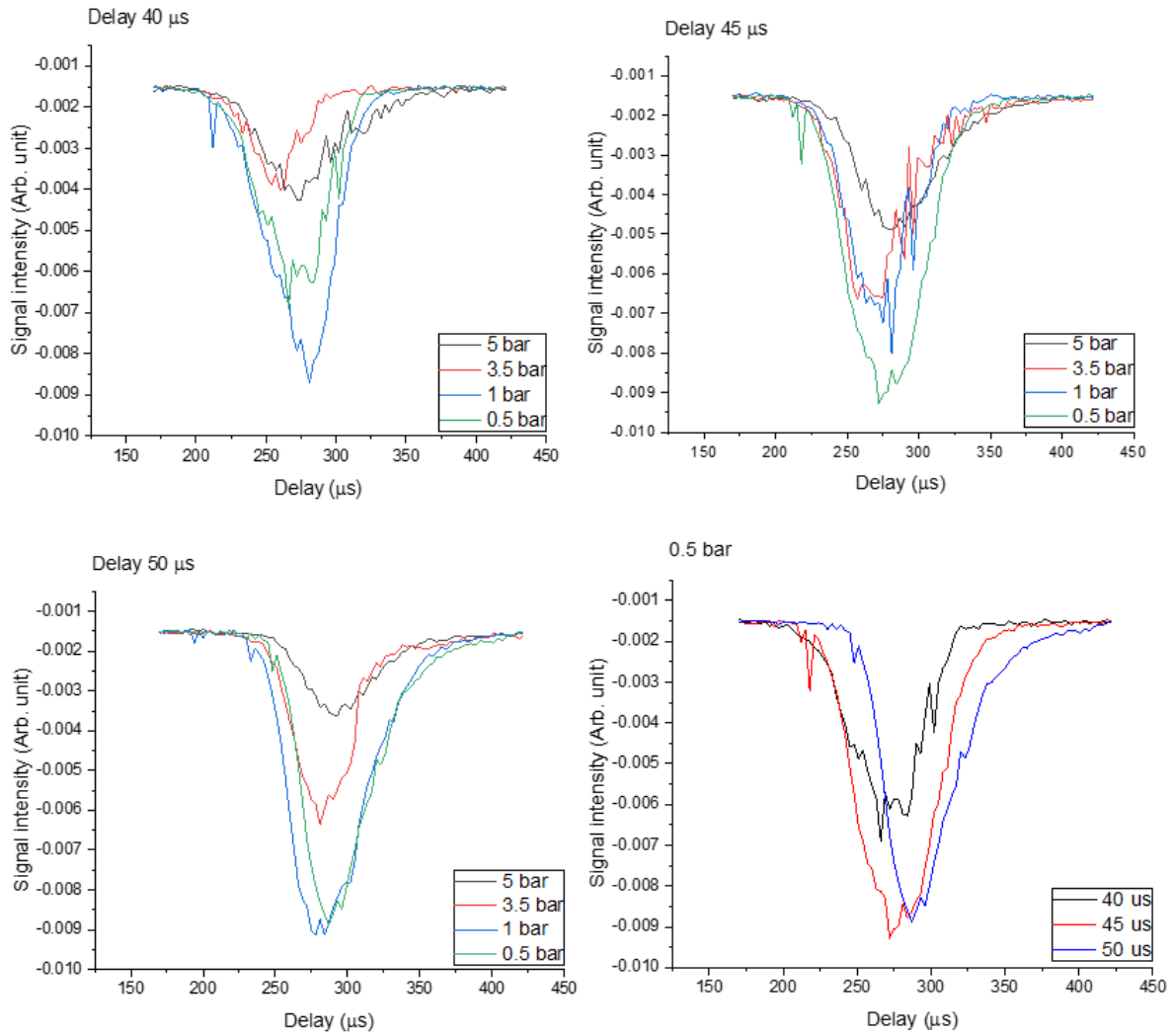

Figure 33: Overview of the backing pressure dependence of the discharge with configuration 1. The backing pressure was measured with a discharge voltage of 920 V and 0.9 mJ laser power (64 avg.)

Subsequently, the voltage dependence of discharge was tested. The results of these measurements are illustrated in figure 31. The lowest measured signal is found at a discharge voltage of 920 volts, for higher voltages the no signal was observed. This is probably caused by the discharge becoming unstable. Therefore, 920 volts is concluded to be the optimum voltage.

Furthermore, the backing pressure of the valve was varied. The results of these measurements are illustrated in figure 33. For delays of 40 μs and backing pressures of $\geq$ 3.5 bar the molecular beam is less stable. At a delay of 50 μs the molecular beams are most stable, which is also the case for a delay of 45 μs with a backing pressure of 0.5 bar. At a discharge delay of 50 μs the beam at 0.5 bar is considered better, due to the smaller width of the beam profile. When comparing the minima at 0.5 bar, a discharge delay of 45 μs seems to be the optimum because the peak is still quite narrow and the intensity is the lowest. It is not surprising to see that the minimum signal intensity is observed at 0.5 bar backing pressure. Because this result is consistent with what was observed in the other two discharge valves which are based on the NPV [7]. However, it is different from the results of the CRUCS valve. The CRUCS valve shows that the minimum OH LIF signal intensity appears when the backing pressure is around 5 bar. Note,

that the nozzle diameter of the pin-hole discharge NPV is around 0.5 mm while the CRUCS valve has an opening of 0.2 mm, which is probably the cause for this difference.

As a conclusion, a backing pressure of 0.5 bar with a discharge delay of 45 μs will form the best suited molecular beam. Also a backing pressure of 1 bar with a discharge delay of 50 μs could be a good candidate. However, this beam profile is broader, which makes the molecular beam less well-defined.

The summarised optimised conditions for configuration 1 are: A discharge delay of 45 μs, a discharge duration of 20 μs, a discharge voltage of 920 volts and a backing pressure of 0.5 bar.

A filament was installed directly after the nozzle (as illustrated in figure 8) in order to improve the production of OH. Beam profiles with the filament at different voltages were measured. Those profiles are shown in figure 34. It follows that the filament stabilises the molecular beam, when going to higher voltages. Hence, the discharge voltage can be increased up to 1.2kV while keeping a stable beam. An increased voltage leads to an decreased intensity and thereby an increased beam density. The beam density was increased by a factor of 1.3. However, this is half the beam density obtained with the CRUCS valve.

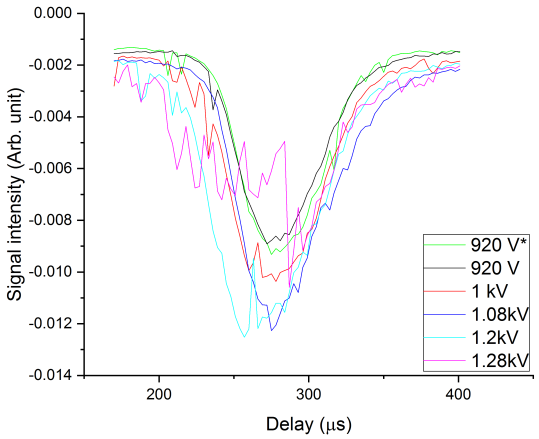

*Figure 34: Overview of the voltage dependence of configuration 1, with filament. The * denotes the beam profile measured without a filament. The measurements were performed at a discharge delay of 50 µs, a discharge duration of 20 µs, 0.6 mJ laser power and 0.5 bar backing pressure(64 avg.)*

Finally the rotationally resolved electronic spectrum was measured, which is depicted in figure 35. Such a spectrum shows transition between different energy states. The energy level diagram of OH and the nomenclature of the transitions are given in appendix A.

In the rotationally resolved electronic spectrum of the molecular beam only transitions from the $X^2\Pi_{\frac{3}{2}}(J = 3/2)$ state are found. Consequently, the molecular beam produced with the new pulsed valve produces molecules which are all in the absolute ground state. The $Q_{21}(1)$ and $Q_1(1)$ transitions, and the $R_{21}(1)$ and $R_1(1)$ transitions show overlap, due to the 0.1 cm^{-1} bandwidth of the used dye laser. However, a double peak, structure of those transitions, is still visible. This result is compared to the rotationally resolved electronic spectrum, figure 6 in reference [7], which is the spectrum of the original NPV with pin-hole discharge. In this spectrum also the first rotationally excited state $J'' = 5/2$ is present. Hence, configuration 1 produces more molecules in the ground state, which is favourable for cold collision experiments.

The difference, of the currently tested valve and the valve we used in reference [7], is the discharge channel as is shown in figure 18. In the original design, a long straight channel was used which is believed to be bad for forming an intense cold beam. In the new design, we get

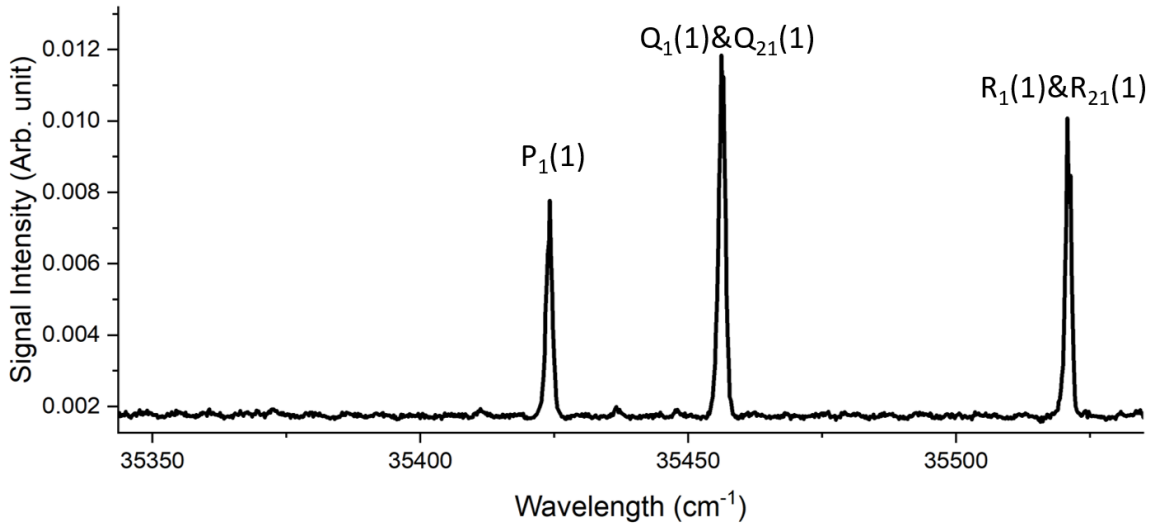

Figure 35: The rotationally resolved electronic spectrum of OH for configuration 1. The peak at 35424.4 cm^{-1} originates from the $P_1(1)$ transition, peak at 35456.2 cm^{-1} originates from the $Q_{21}(1)$ and $Q_1(1)$ transition, peak at 35520.8 cm^{-1} originates from the $R_{21}(1)$ and $R_1(1)$ transition. This spectrum was measured with a discharge delay of 50 µs, discharge duration of 20 , 1.08 KV, 0.5 bar backing pressure and 0.9 mJ laser power (16 avg.)

rid of the straight channel and keep the cone shape all the way down to the nozzle. This design has the advantage that it has the ideal nozzle shape with the cost of larger discharge electrode diameters which will make the discharge less efficient at the same voltage applied on the old pin-hole discharge valve design. This point will be discussed in more detail in the following section.

The new pin-hole discharge design was not yet compared to the original used design. Hence, this comparison will be made in the near future. Also, the effect of the discharge being directed towards the valve body was not yet studied.

9.2 Configuration 2

For the second configuration the same approach is used as for configuration 1. Configuration 2 has the high voltage plate further away from the o-ring, with respect to configuration 1. Furthermore, this configuration has the same order of the plates as for the NPV with original pin-hole discharge design. Hence, by optimising and comparing this new design, the effect of the difference in shape is found.

First the discharge duration and delay were optimised. The discharge delay was varied from 30 to 60 μs and the discharge duration was varied from 20 to 40 μs. In figure 36 these measurements are shown. It becomes even more clear than in figure 32, that the width of the peaks decreases with shorter duration of the discharge. From figure 36 we can also conclude that a discharge delay of 40 μs and 50 μs will lead to the lowest signal intensity. For a discharge delay of 40 μs, a minimal signal intensity is found at a discharge duration of 40 μs. Although this peak is quite broad, it is stable. For a discharge delay of 50 μs a discharge duration of 35 μs will lead to the lowest signal, this peak is less broad but also less stable. Hence, depending on the aim of the experiment one of those options will be suited. For the aim to of producing a stable molecular beam a discharge delay of 40 μs, with a discharge duration of 40 μs is best suited.

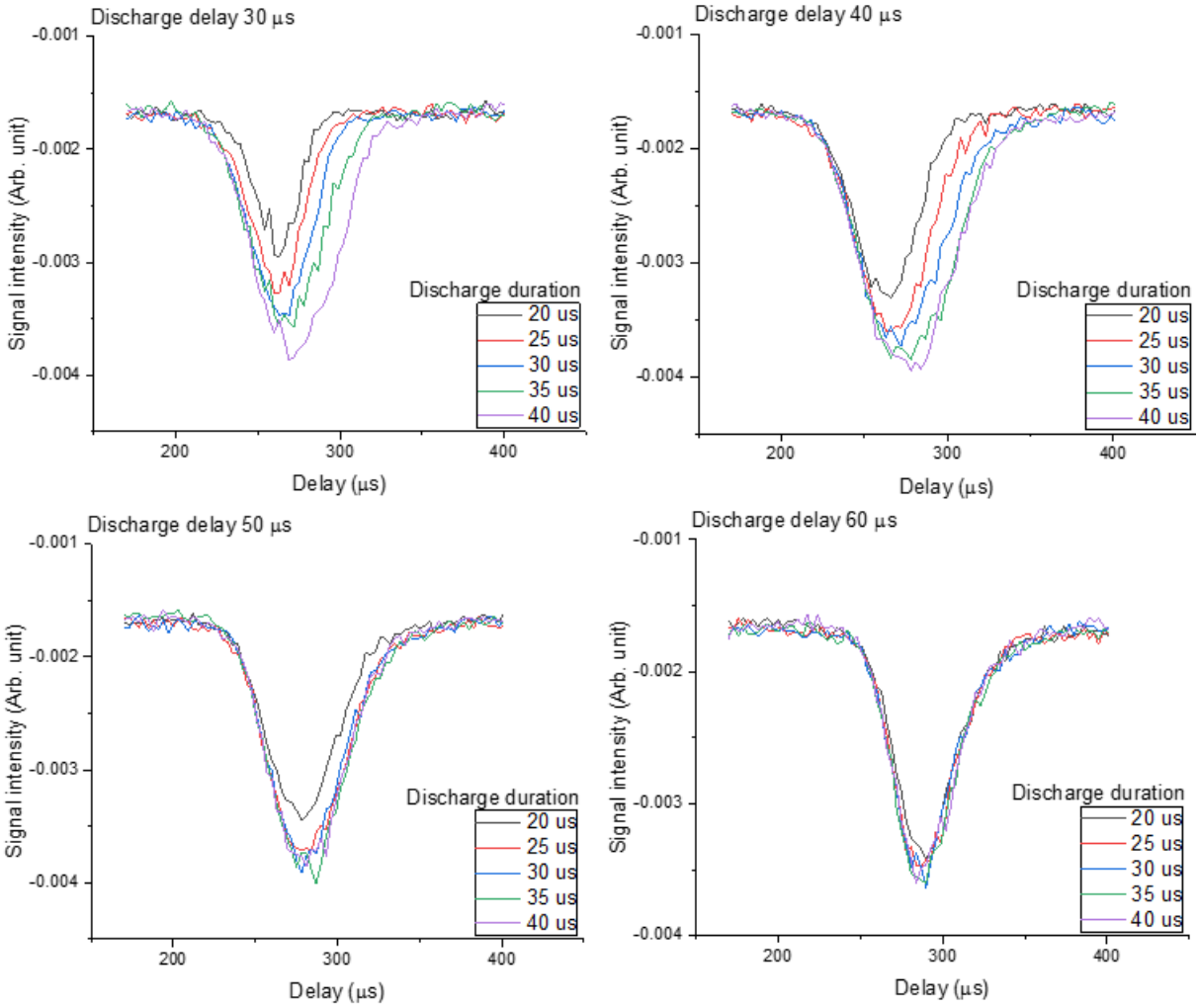

Figure 36: Overview of the different discharge durations with varying discharge delay of configuration 2. The signals were measured with a backing pressure of 0.5 bar, 900 V and 0.8 mJ laser power (16 avg.).

Then, the voltage dependence of the discharge of configuration 2 was measured. The results of these measurements are shown in figure 37. From this figure becomes clear that the optimal discharge voltage is 1 kV.

Subsequently, the backing pressure is varied. This measurement is done for a discharge delay of 50μs (A) and 40μs (B). The results are illustrated in figure 38. From these measurements it becomes clear that for both discharge delays, a backing pressure of 1 bar will lead to a higher beam density. From those options a discharge delay of 40 μs and discharge duration of 40 μs gives the lowest signal.

Consequently, the optimum conditions for configuration 2 are a discharge delay of 40 μs and a discharge duration of 40 μs with a discharge voltage of 1 kV and a backing pressure of 1 bar.

What is striking however, is the increased signal intensity compared to configuration 1 (without filament), when all the variables are optimised. The increased signal intensity is probably caused by the increased diameter of the high voltage metal plate, and the distance with respect to the nozzle. Because the discharge occurs further away from the nozzle and the molecular

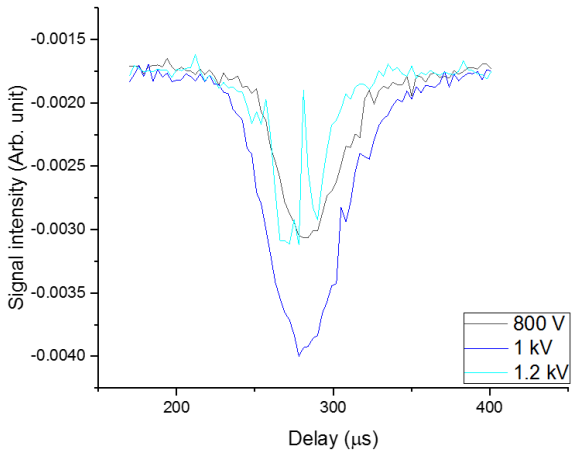

Figure 37: The voltage dependence of configuration 2. Measured at a discharge delay of 50 µs, a discharge duration of 30 µs, 0.5 backing pressure and 0.9 mJ laser power (16 avg.)

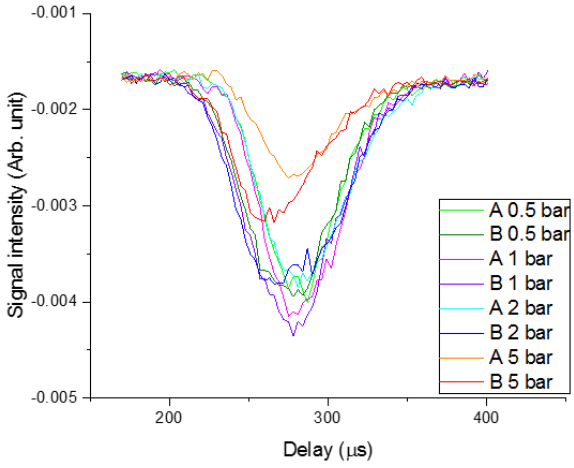

Figure 38: The backing pressure dependence of configuration 2, for the two highest signal discharge set-up. A: discharge delay: 50 µs and discharge duration: 35 µs. B: discharge delay: 40 µs and discharge duration: 40 µs. These profiles were measured with 5 bar backing pressure, 900V and 0.87 mJ laser power (16 avg.)

beam could expand, the density H_2O molecules is decreased. Hence, the number of dissociated H_2O molecules is lowered and thereby the number of created OH molecules is decreased. Therefore, in experiments where a high beam density is needed, the first configuration is a better option.

The filament was added to the test chamber, and new voltage dependence measurements were performed. The results of these measurements are illustrated in figure 39. For this configuration the addition of the filament has a significant effect. The filament makes it possible to increase the voltage by a factor of 1.8. Therefore the signal intensity was significantly lowered. A voltage of 1.7 kV can be achieved. However 1.6 kV is preferred, because this molecular beam is still stable and the signal intensity is approximately equal.

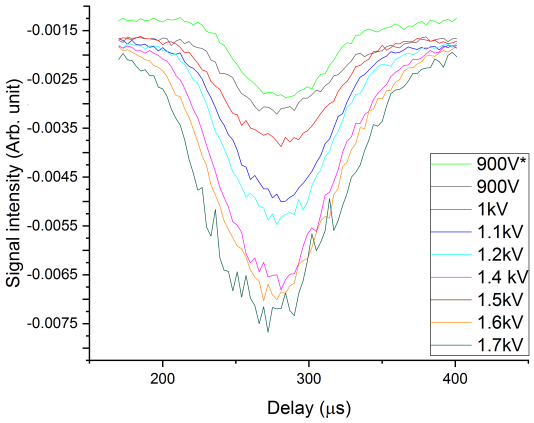

*Figure 39: Overview of the voltage dependence of configuration 2 with a filament. The * denotes the beam profile measured without a filament. The measurements were performed at a discharge delay of 40 µs, discharge delay of 40 µs, 1 bar backing pressure and a laser power of 0.6 mJ (64 avg.).*

Although, the voltage for this configuration is increased much more than for configuration 1, configuration 1 has a 1.5 times lower signal intensity. Consequently, configuration 1 produces OH molecular beams with a much higher beam density. Furthermore, for both configurations is observed that a change in voltage, does not alter the optimum discharge duration and discharge delay. The

reason for this observation is that the molecular beam velocity remained equal. Therefore, the molecules arrive at the same time at the region where the discharge occurs. Hence, it was expected that the discharge duration and discharge delay did not change.

Finally, the rotationally resolved electronic spectrum of the molecular beam formed by configuration 2 was measured. The result of this measurement is depicted in figure 40. The laser power used for the rotationally resolved spectrum is lower with respect to the measurement for configuration 1. However, the signal was saturated at 0.4mJ. So this difference does not lead to a difference in the rotationally resolved spectrum. Also, for configuration 2 only transitions of the $X^2\Pi_{\frac{3}{2}}(J = 3/2)$ are found.

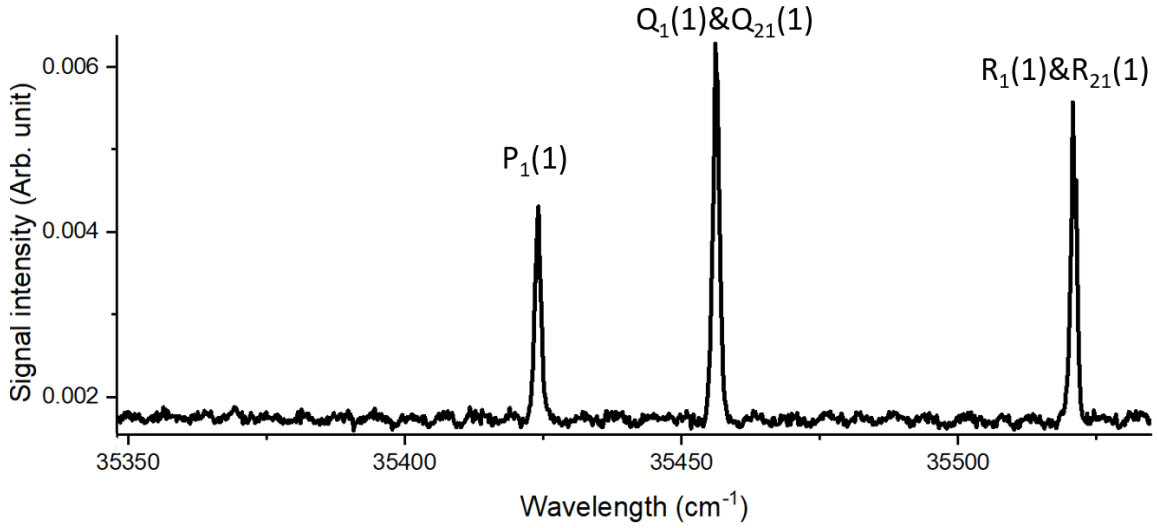

Figure 40: The rotationally resolved electronic spectrum of OH for configuration 2. Peak at 35424.4 cm^{-1} originates from the $P_1(1)$ transition, peak at 35456.1 cm^{-1} originates from the $Q_{21}(1)$ and $Q_1(1)$ transition, peak at 35520.8 cm^{-1} originates from the $R_{21}(1)$ and $R_1(1)$ transition. The rotationally resolved electronic spectrum was measured with a discharge delay of 40 , discharge duration of 40 , 1.6 kV, 1 bar backing pressure and 0.6 mJ laser power (16 avg.)

As stated before, the total beam density for configuration 2 is much lower than that of configuration 1. However, the produced beam is an improvement with respect to the previously used design of the NPV with pin-hole discharge from reference [7], because it produces colder molecular OH beams. For the above mentioned new pin-hole discharge design, no comparison was made with the original valve with respect to the beam density. Furthermore, because configuration 1 provides a higher beam density, only this configuration will be compared to the original pin-hole discharge design. In order to compare the two designs, the original design will be measured on the same experimental set-up in the near future.

Part VI
Conclusion and Prospect

This thesis shows the optimisation of molecular beam sources for two different types of collision experiments. First, the NO and H_2 molecular beams were optimised for crossed molecular beam experiments. The beams were optimised in order to measure at collision energies in the range $1.5 - 10cm^{-1}$. In this range the aim is to measure ICSs and DCSs in order to verify theories that describe the interaction between NO and H_2 molecules. Secondly, two new designs of the NPV equipped with pin-hole discharge were optimised and compared (figure 19). This with the aim of producing a better suited OH molecular beam for trapping experiments.

In order to obtain the lowest collision energy for NO-H_2 collisions and thereby observe quantum mechanical effects such as scattering resonances, the H_2 and NO molecular beams were optimised. The minimum velocity of the H_2 molecular beam that could be reached is 800 m/s. From velocity of H_2 and the NO gas mixtures (table 2) collision energies in the range of $1.5 - 11.5cm^{-1}$ can in principle be reached. Furthermore, an ICS of the 1/2e channel was measured (figure 25). Also, an angular distribution of scattering products was measured (figure 26). Both of these measurements were measured with an *n*-hydrogen mixture. For collision experiments with only *p*-hydrogen, DCSs at different collision energies were simulated.

So far a lot has been achieved, in the study of collisions between the NO and H_2 molecules. A next step is to measure more detailed ICSs and DCSs. Furthermore, a more precise determination of the velocity spread of the molecular beams will be performed. The next aim is to measure more ICSs and DCSs for collisions with *p*-hydrogen in the near future.

Furthermore, two new designs for the NPV with pin-hole discharge were optimised. From the optimised conditions one can conclude that configuration 1 will lead to better suited OH molecular beams for trapping experiments, due to the increased amount of the beam density, with respect to configuration 2. Subsequently, the new designs of the NPV with pin-hole discharge are an improvement for producing colder molecular beams. Also was concluded that for the new designs the addition of a filament had a remarkable effect on the voltage that can be reached, while keeping a stable molecular beam.

A next step will be to measure the original pin-hole discharge design on the same test chamber. Then the signal intensities could be compared to see whether the beam density is also improved by this new design. Another option is to make the test chamber suitable for performing beam density measurements. After the comparison between the NPVs with pin-hole discharge can be concluded whether the new design will be better suited, and therefore whether it will be implemented in the experiments or not.

Altogether, the presented results show the enormous versatility of molecular beams and their significant effect on molecular collision experiments.

Part VII

Bibliography

[1] G. Scoles; D. Bassie; U. Buck; D. Laine. *Atomic and Molecular Beam Methods*, volume 1. Oxford University Press, 1988.

[2] J. Onvlee; S.N. Vogels; S.Y.T. van de Meerakker. Unraveling Cold Molecular Collisions: Stark Decelerators in Crossed-Beam Experiments. *ChemPhysChem. Reviews*, **17**(22), 2016.

[3] S.N. Vogels. *Imaging high-resolution cold & controlled molecular collisions*. PhD thesis, Radboud University, 2017.

[4] T. de Jongh; T. Karman; S.N. Vogels; M. Besemer; et. al. Imaging diffraction oscillations for inelastic collisions of NO radicals with He and D_2. *The Journal of Chemical Physics*, **147**(0139418), 2017.

[5] S.Y.T. van de Meerakker; H.L. Benthlem; N. Vanhaekcke; G. Meijer. Manipulation and Control of Molecular Beams. *American Chemical Society*, **112**(9), 2012. Chemical Reviews.

[6] B. Yan; P.F.H. Claus; B.G.M. van Oorschot; L. Gerritsen; A.T.J.B. Eppink; S.Y.T. van de Meerakker; D.H. Parker. A new high intensity and short-pulse molecular beam valve. *Review of Scientific Instruments*, **84**(023102), 2013.

[7] L. Ploenes; D. Haas; D. Zhang; S.Y.T. van de Meerakker; S. Willitsch. Cold and intense OH radical beam sources. *Review of Scientific Instruments*, **87**(053305), 2016.

[8] J. Onvee; S.N. Vogels; A. von Zastrow; D.H. Parker; S.Y.T. van de Meerakker. Molecular Collisions coming into focus. *Phys. Chem. Chem. Phys.*, **16**(15768), 2014.

[9] S. Wilson; R. Appleton. *Handbook of Molecular Physics and Quantum Chemistry*, volume 3. John Wiley Amp; Sons Inc, 2003.

[10] M. Kirste. *OH-NO Scattering at the Quantum level*. PhD thesis, Fritz-Haber-Institut der Max-Planck-Gesellschaf, 2012.

[11] D.A. McQuarrie. *Quantum Chemistry*. University Science Books, 2nd edition.

[12] H.W. Woolley; R.B. Scott; F.G. Brickwedde. Compilation of thermal properties of hydrogen in its various isotopic and ortho-para modifications. *Journal of Research of the National Bureau of Standards*, **41**(5), 1948.

[13] J. J. ter Meulen; W. L. Meerts; G. W. M. van Mierlo; A. Dymanus. Observations of Population Inversion between the Λ-Doublet States of OH. *Phys. Rev. Lett.*, **36**(17), 1976.

[14] M.P. Docker; A. Hodgson; J.P. Simons. Photodissociation of H_2O_2 at 248 nm: translational anisotropy and oh product state distributions. *Phys. Rev. Lett.*, **128**(3), 1986.

[15] S.Y.T. van de Meerakker. *Deceleration and Electrostatic Trapping of OH radicals*. PhD thesis, Radboud University Nijmegen, 2006.

[16] J. Onvlee. *Unraveling Molecular Collisions, Experiment and Theory*. PhD thesis, Radboud University Nijmegen.

[17] S. Chefdeville; Y. Kalugine; S.Y.T. vand Meerakker; C. Naulin; F. Lique; M. Costes. Observation of Partial Wave Resonances in Low-Energy O_2-H_2 Inelastic Collisions. *Science*, **341**(6150), 2013.

[18] B.H. Brandsden; C.J. joachain. *Quantum Mechanics*. Pearson, 2nd edition, 2000.

[19] M. Brouard; C. Vallance, editor. *Tutorials in Molecular Reaction Dynamics*. The Royal Society of Chemistry, 2012. Chapter 1, 5 and 12.

[20] B. H. Bransden; C. J. Joachain. *Quantum mechanics*. Pearson Education Limited, 2nd edition, 2000.

[21] P. Atkins; R. Friedman. *Molecular quantum mechanics, fourth edition*. Oxford University Press, 2005.

[22] J.P. Toennies; W. Welz; G. Wolf. Molecular beam scattering studies of orbiting resonances and the determination of van der Waals potentials for H-Ne, Ar, Kr and Xe and for H_2-Ar, Kr and Xe. *The journal of Chemical Physics*, **71**(2), 1979.

[23] S.N. Vogels; J. Onvlee; S. Chefdeville; A. van der Avoird; G.C. Groenenboom; S.Y.T. van de Meerakker. Supplementary Material for; Imaging resonances in low-energy NO-He inelastic collisions. *Science*, **350**(787), 2015.

[24] S.Y.T. van de Meerakker; H.L. Benthlem; G. Meijer. Taming molecular beams. *Nature physics*, **4**(595), Augustus 2008. Chemical reviews.

[25] T. Cremers; S. Chefdeville; N. Janssen; E. Sweers; S. Koot; K. Claus; S.Y.T. van de Meerakker. Multistage Zeeman decelerator for molecular-scattering studies. *Phys. Rev. A*, **95**(4), Apr 2017.

[26] U. Even. The Even-Lavie valve as a source for high intensity supersonic beam. *EPJ Techniques and Instrumentation*, **2**(1), Dec 2015.

[27] W. Christen; K. Rademann. Cooling and slowing in high-pressure jet expansions. *Phys. Rev. A.*, **77**(012702), 2008.

[28] L. Scharfenberg; S.Y.T. van de Meerakker; G. Meijer. Crossed beam scattering experients with optimized energy resolution. *Phys.Chem.Chem.Phys*, **13**(18), 2011.

[29] A.T.J.B. Eppink; D.H. Parker. Velocity map imaging of ions and electrons using electrostatic lenses: Application in photoelectron and photofragment ion imaging of molecular oxygen. *Review of Scientific instruments*, **68**(3477), 1997.

[30] A. Zastrow; J. Onvlee; S.S. Vogels; et al. State-resolved diffraction oscillations imaged for inelastic collisions of NO radicals with He, Ne and Ar. *Nature Chemistry*, **6**(216), 2014.

[31] A. Zastrow; J. Onvlee; S.S. Vogels; et al. Supplementary: State-resolved diffraction oscillations imaged for inelastic collisions of NO radicals with He, Ne and Ar. *Nature Chemistry*, **6**(216), 2014.

[32] U. Even. Pulsed Supersonic Beams form High Pressure Source: Simulations Results and Experimental Measurements. *Advances in Chemistry*, **2014**(636042), 2014.

[33] S.N. Vogels; J. Onvlee; S. Chefdeville; A. Avoird; G.C. Groeneboom; S.Y.T. Meerakker. Imaging resonances in low-energy NO-He inelastic collisions. *AAAS*, **350**(6262), 2015.

[34] van Itterbeek; Verbeke et al. The Difference in Vapour Pressure Between Normal and Equilibrium Hydrogen. Vapour Pressure of Normal Hydrogen Between 20K and 32K. *Physica*, **30**(6), 1964.

[35] J. Klos; et. al. The interaction of NO($X^2\Pi$) with H_2: Ab initio potential energy surfaces and bound states. *J. Chem. Phys.*, **146**(114301), 2017.

[36] C. Naulin; N. Daugey; K.M. Hickson; M. Costes. Dynamics of the Reactions of C(^3P_J) Atoms with Ethylene, Allene, and Methylacetylene at Low Energy Revealed by Doppler-Fizeau Spectroscopy. *J. Phys. Chem.*, **113**(144447), 2009.

[37] D. R. Yarkony. A theoretical treatment of the predissociation of the individual rovibronic levels of OH/OD($A^2\Sigma^+$). *The Journal of Chemical Physics*, **97**(1838), 1992.

[38] G.H. Dieke; H.M. Crosswhite. The ultraviolet bands of OH. *Journal of Quantitative Spectroscopy and Radiative Transfer*, **2**(2), 1962.

Part VIII
Appendices

Appendix A

The energy level diagram of the vibrational ground states of the electronic ground states $X^2\Pi$ and first excited state $A^2\Sigma$ of OH

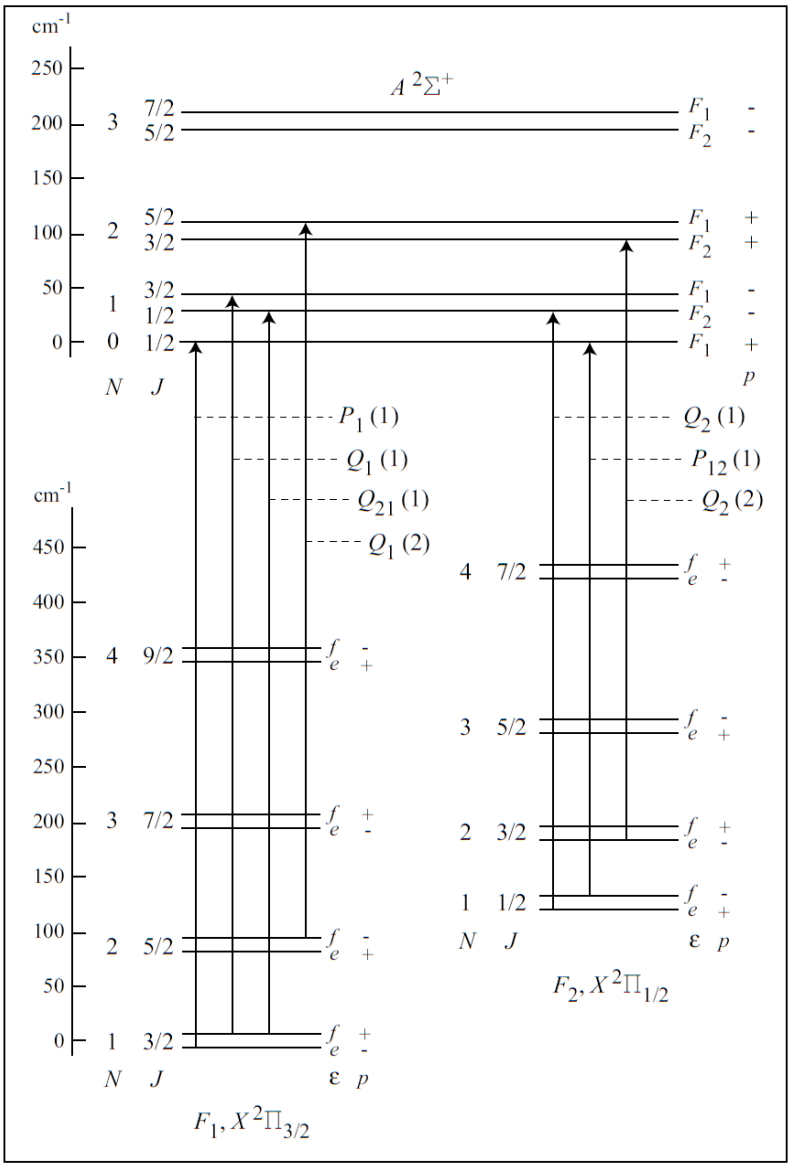

Figure 41: Here: $\Delta N_{F'F''}(N'')$, is used for the labelling for the transition states. (Adapted from reference [15])

Transitions between energy levels are labelled with: $\Delta N_{F'F''}(N'')$
Here ΔN denotes the transitions between different values of quantum number N. ΔN = -2 (O), -1 (P), 0 (Q), +1 (R), +2 (S). Where the letters are used in the labelling system for ΔN. F' denotes the i value of the final F_i state of the transition. F'' denotes the initial F_i value value of the transition. When $F' = F''$ only one subscript is indicated. The initial value of quantum number N of the transition is indicated by N''. [15] [38]